

The influence of hydrogen on the chemical, mechanical, optical/electronic, and electrical transport properties of amorphous hydrogenated boron carbide

Bradley J. Nordell, Sudarshan Karki, Thuong D. Nguyen, Paul Rulis, A. N. Caruso, Sudhaunshu S. Purohit, Han Li, Sean W. King, Dhanadeep Dutta, David Gidley, William A. Lanford, and Michelle M. Paquette

Citation: *Journal of Applied Physics* **118**, 035703 (2015); doi: 10.1063/1.4927037

View online: <http://dx.doi.org/10.1063/1.4927037>

View Table of Contents: <http://scitation.aip.org/content/aip/journal/jap/118/3?ver=pdfcov>

Published by the [AIP Publishing](#)

Articles you may be interested in

[Effects of condensation reactions on the structural, mechanical, and electrical properties of plasma-deposited organosilicon thin films from octamethylcyclotetrasiloxane](#)
J. Appl. Phys. **97**, 113707 (2005); 10.1063/1.1923163

[Dielectric properties of amorphous hydrogenated silicon carbide thin films grown by plasma-enhanced chemical vapor deposition](#)
J. Appl. Phys. **93**, 4066 (2003); 10.1063/1.1555676

[Intermittent chemical vapor deposition of thick electrically conductive diamond-like amorphous carbon films using i- C 4 H 10 / N 2 supermagnetron plasma](#)
J. Vac. Sci. Technol. A **20**, 403 (2002); 10.1116/1.1446446

[Influence of the plasma pressure on the microstructure and on the optical and mechanical properties of amorphous carbon films deposited by direct current magnetron sputtering](#)
J. Vac. Sci. Technol. A **17**, 2841 (1999); 10.1116/1.582022

[Effects of deposition temperature on the properties of hydrogenated tetrahedral amorphous carbon](#)
J. Appl. Phys. **82**, 4566 (1997); 10.1063/1.366193



SHIMADZU Excellence in Science **Powerful, Multi-functional UV-Vis-NIR and FTIR Spectrophotometers**

Providing the utmost in sensitivity, accuracy and resolution for a wide array of applications in materials characterization and nanotechnology research

- Photovoltaics
- Polymers
- Thin films
- Paints/inks
- Ceramics
- FPDs
- Coatings
- Semiconductors

[Click here to learn more](#)



The influence of hydrogen on the chemical, mechanical, optical/electronic, and electrical transport properties of amorphous hydrogenated boron carbide

Bradley J. Nordell,¹ Sudarshan Karki,¹ Thuong D. Nguyen,¹ Paul Rulis,¹ A. N. Caruso,¹ Sudhaunshu S. Purohit,² Han Li,³ Sean W. King,³ Dhanadeep Dutta,^{4,a)} David Gidley,⁴ William A. Lanford,⁵ and Michelle M. Paquette^{1,b)}

¹Department of Physics and Astronomy, University of Missouri-Kansas City, Kansas City, Missouri 64110, USA

²Department of Chemistry, University of Missouri-Kansas City, Kansas City, Missouri 64110, USA

³Logic Technology Development, Intel Corporation, Hillsboro, Oregon 97124, USA

⁴Department of Physics, University of Michigan, Ann Arbor, Michigan 48109, USA

⁵Department of Physics, University at Albany, Albany, New York 12222, USA

(Received 27 April 2015; accepted 7 July 2015; published online 20 July 2015)

Because of its high electrical resistivity, low dielectric constant (κ), high thermal neutron capture cross section, and robust chemical, thermal, and mechanical properties, amorphous hydrogenated boron carbide ($a\text{-B}_x\text{C:H}_y$) has garnered interest as a material for low- κ dielectric and solid-state neutron detection applications. Herein, we investigate the relationships between chemical structure (atomic concentration B, C, H, and O), physical/mechanical properties (density, porosity, hardness, and Young's modulus), electronic structure [band gap, Urbach energy (E_U), and Tauc parameter ($B^{1/2}$)], optical/dielectric properties (frequency-dependent dielectric constant), and electrical transport properties (resistivity and leakage current) through the analysis of a large series of $a\text{-B}_x\text{C:H}_y$ thin films grown by plasma-enhanced chemical vapor deposition from *ortho*-carborane. The resulting films exhibit a wide range of properties including H concentration from 10% to 45%, density from 0.9 to 2.3 g/cm³, Young's modulus from 10 to 340 GPa, band gap from 1.7 to 3.8 eV, Urbach energy from 0.1 to 0.7 eV, dielectric constant from 3.1 to 7.6, and electrical resistivity from 10¹⁰ to 10¹⁵ Ω cm. Hydrogen concentration is found to correlate directly with thin-film density, and both are used to map and explain the other material properties. Hardness and Young's modulus exhibit a direct power law relationship with density above ~ 1.3 g/cm³ (or below $\sim 35\%$ H), below which they plateau, providing evidence for a rigidity percolation threshold. An increase in band gap and decrease in dielectric constant with increasing H concentration are explained by a decrease in network connectivity as well as mass/electron density. An increase in disorder, as measured by the parameters E_U and $B^{1/2}$, with increasing H concentration is explained by the release of strain in the network and associated decrease in structural disorder. All of these correlations in $a\text{-B}_x\text{C:H}_y$ are found to be very similar to those observed in amorphous hydrogenated silicon ($a\text{-Si:H}$), which suggests parallels between the influence of hydrogenation on their material properties and possible avenues for optimization. Finally, an increase in electrical resistivity with increasing H at $<35\%$ H concentration is explained, not by disorder as in $a\text{-Si:H}$, but rather by a lower rate of hopping associated with a lower density of sites, assuming a variable range hopping mechanism interpreted in the framework of percolation theory. © 2015 AIP Publishing LLC.

[<http://dx.doi.org/10.1063/1.4927037>]

I. INTRODUCTION

Research on low- Z boron-rich boron carbide (BC) materials continues to be motivated by their unique mechanical, thermal, chemical, optical, and electronic properties.^{1–6} In particular, thin-film boron carbide has emerged as a promising moderately high bandgap (2–4 eV) semi-insulating nanoelectronic material for direct-conversion solid-state neutron detectors^{7–11} and low-dielectric-constant (low- κ) intra/interlayer

dielectrics,^{12,13} as well as a candidate material for specialized coatings.^{14–17} For these and other applications to reach technological maturity, a greater understanding of the relationship between chemical structure and technologically relevant material properties, and how these can ultimately be controlled by processing conditions, is essential.

A variety of techniques have been developed to fabricate boron-carbide-based solids,^{18,19} with the resulting materials spanning the BC(H) phase diagram^{5,20,21} and potential energy landscape.²² Growth techniques such as pressure and pressureless sintering, hot pressed pellet, and hot isostatic pressing,^{23–25} which apply high growth temperatures ($T > 2200$ °C) and/or pressures ($P > 50$ Torr), have been used

^{a)}Current address: Radiochemistry Division, Bhabha Atomic Research Centre, Trombay, Mumbai 400 085, India.

^{b)}Author to whom correspondence should be addressed. Electronic mail: paquettem@umkc.edu

to produce single or polycrystalline B_xC , typically with a stoichiometry of $\sim B_4C$, exhibiting the extreme properties needed for traditional applications such as armor and abrasives. The problem with employing such bulk growth techniques for the specialized semiconductor device applications described above is that they require harsh fabrication conditions, demonstrate limited tunability, and tend to yield unfavorable electronic properties such as unacceptably high electrical conductivity.^{26,27} It has been demonstrated^{28–34} that the use of thin-film fabrication methods such as chemical vapor deposition or physical vapor deposition can produce B_xC thin films that maintain robust mechanical, thermal, and chemical properties, while improving on electrical transport, electronic, and/or optical properties (e.g., resistivity and band gap), without having to resort to the extreme conditions required by traditional bulk growth techniques. In particular, the plasma-enhanced chemical vapor deposition (PECVD) of films from *ortho*-carborane ($o-C_2B_{10}H_{12}$), which typically yields amorphous hydrogenated boron carbide ($a-B_xC:H_y$) when lower growth temperatures are used, has been shown to be suitable for producing films for device applications as well as conducive to tuning properties over a wide range.^{35–44} With tunability, however, comes complexity, and although the ability to vary properties bodes well for optimizing a material system, there has neither been an extensive study on just how variable these properties can be nor an emphasis on understanding their physical underpinnings. Such investigations will be critical if boron-carbide-based materials are to meet the stringent material requirements for next-generation technologies.

The trajectory of PECVD amorphous hydrogenated silicon ($a-Si:H$) represents a compelling example of a technological maturation process whereby many years of focused study on a material led to its eventual integration into a number of commercial applications, both anticipated and unforeseen.⁴⁵ A key finding in the history of $a-Si:H$ was realizing the importance of hydrogenation in passivating dangling bonds and decreasing disorder. Within the amorphous silicon literature, hundreds of papers have been and continue to be published on the topic of hydrogen alone, covering its influence on microstructure, electronic and optical properties, photodegradation, and more. The improvements in semiconducting properties that resulted from better understanding and optimizing $a-Si:H$ allowed for its deployment in solar cells, active-matrix liquid crystal displays, and other large-area electronics.^{46,47} Although $a-B_xC:H_y$ is still relatively new on the electronic materials scene, we anticipate that similar focused research efforts may set this material up for similar—if more modest—successes.

Herein, we investigate the relationship between chemical, mechanical, electronic/optical, and electrical transport properties in thin-film $a-B_xC:H_y$. We apply a hybrid factorial/response surface experiment design to produce a large series of films of varying chemical composition and properties by modifying temperature and power in the PECVD growth of $a-B_xC:H_y$ from *ortho*-carborane. We measure a wide range of properties, including B/C ratio, hydrogen and oxygen content, density, pore diameter, Young's modulus, hardness, band gap, Urbach energy, Tauc slope parameter,

dielectric constant (high- and low-frequency), electrical resistivity, and leakage current. From these results, we demonstrate that hydrogen concentration can serve as a useful proxy for many important material properties in $a-B_xC:H_y$. We analyze the effects of hydrogenation in the context of the accumulated knowledge bank for a series of well-known amorphous solids, $a-Si:H$, $a-C:H$, and $a-SiC:H$, and show how parallel phenomena can guide us to pathways for material property optimization.

II. EXPERIMENTAL DETAILS

All thin-film $a-B_xC:H_y$ samples reported in this work were prepared in a custom-built parallel-plate capacitively coupled PECVD system with *ortho*-carborane ($o-C_2B_{10}H_{12}$) precursor and argon working gas. The reactor system, which differs from commercial systems due to the use of an inverted, rotating substrate holder/heater, consists of a 12 cm diameter upper rotating anode, acting as substrate holder, and 25 cm diameter lower cathode, separated from the anode by 4.4 cm, acting as precursor dispersion and delivery system (also known as the showerhead) housed within an 80 l chamber operating at a base pressure of $\sim 5 \times 10^{-7}$ Torr. The substrate heating system comprises an SHQ400 series rotating substrate heater from AJA International controlled by a PTB SHQ-15A PID controller. The actual temperature of the substrate holder has been independently calibrated in reference to the temperature controller readout. A motorized rotary feedthrough allows for substrate rotation of up to 20 rpm to facilitate heating and deposition uniformity. R.F. power is delivered at a standard frequency of 13.56 MHz via an ACG-5 XL R.F. plasma generator and MW-5 automatic matching network.

The base of the showerhead is connected via feedthrough to a solid precursor “bubbler” (for sublimation) and flow rate control system. The bubbler consists of a glass nipple containing a stack of glass beads above which is loaded *ortho*-carborane powder on top of a mesh screen. Heated Ar gas is flowed through the bubbler to deliver sublimed *ortho*-carborane to the showerhead. The flow rate of the argon is controlled by an MKS mass flow controller (0–200 sccm), but the precise concentration of *ortho*-carborane within the argon/*ortho*-carborane mixture is unknown. The argon gas lines and showerhead are heated to 90 °C and the bubbler to 75 °C. The *ortho*-carborane is sourced from Katchem Ltd., resublimed *in vacuo* prior to use, and loaded into the bubbler under inert conditions. Process argon gas is sourced from Airgas Inc. (BIP grade) with a specified purity of 99.9999% (<10 ppb O_2 and <20 ppb H_2O). High-capacity Restek O_2 and H_2O filters are installed in line to further reduce oxygen and water impurity levels to the hundreds-of-ppt range.

A series of $a-B_xC:H_y$ films were grown starting from one-factor and two-factor designs by varying growth temperature and R.F. power, and filling in additional data points in the regions of interest. The result was a response surface matrix of twenty-eight growths spanning growth temperatures of 50–450 °C and R.F. powers of 5–30 W (Table I, Fig. 1), with the remaining PECVD conditions held constant. Films were grown for thirty minutes at a pressure of 200 mTorr,

TABLE I. Summary of thin-film properties for a series of a-B_xC:H_y samples grown by plasma-enhanced chemical vapor deposition from *ortho*-carborane with varying growth temperature and power.^a

Film	Temp (°C)	Power (W)	d^b (nm)	Density (g/cm ³) ^c	%H ^e	%B ^c	%C ^c	%O ^c	B/C	H^d (GPa)	E^d (GPa)	Pore diam. (nm) ^e	E_{Tauc}^f ($n=2/3$) (eV)	E_{04}^f (eV)	E_U^f (meV)	$B^{1/2f}$ (eV cm) ^{-1/2}	ϵ_1^b (10 ¹⁴ Hz)	κ^g (10 ⁶ Hz)	ρ^h (Ω cm)
D1	152	20	557	2.9/2.4	3.9	512	194	3.2	4.1	1 × 10 ¹²
D2	232	20	795	1.50	34	55	11	0	4.9	2.7/2.0	3.2	513	282	3.4
D5	272	20	590	1.58	32	57	12	0	4.8	11	144	...	2.5/2.0	3.0	592	314	3.5	4.1	7 × 10 ¹²
D8	312	20	577	1.64	29	59	12	0	4.9	13	183	...	2.4/1.8	2.7	607	334	3.9	4.6	1 × 10 ¹³
D10	292	20	757	2.7/1.9	3.2	583	292	3.3	...	5 × 10 ¹³
D11	52	20	550	0.98	42	47	11	11	4.3	0.61	2.3	3.2	1 × 10 ¹²
D12	392	10	643	1.41	35	53	12	3	4.6	9	116	...	3.5/3.2	3.6	359	678	3.5	4.1	4 × 10 ¹⁴
D13	112	30	403	1.40	36	53	11	1	4.6	1	12	...	3.4/3.0	3.3	479	793	3.6	4.0	1 × 10 ¹³
D14	112	10	407	3.7/3.4	3.8	149	1249	2.9
D15	72	10	442	1.05	45	43	10	8	4.2	1	15	0.59	3.8/3.5	3.9	171	1230	2.4	3.8	1 × 10 ¹²
D16	52	5	477	3.8/3.5	3.8	118	1650	2.3	3.4	1 × 10 ¹⁴
D17	152	5	712	1.24	41	48	10	4	4.8	1	19	0.59	3.7/3.5	3.8	208	1043	2.9	4.5	1 × 10 ¹²
D18	72	15	260	0.92	44	44	13	6	3.5	1	27	0.69	3.7/3.5	3.8	176	1640	2.3	4.3	5 × 10 ¹³
D19	72	25	205	0.96	44	44	13	5	3.5	1	25	0.69	109	...	2.5	3.1	1 × 10 ¹⁴
D20	112	20	311	1.20	40	48	11	4	4.3	2	25	0.63	3.6/3.4	3.7	189	1428	2.9	4.1	...
D21	152	25	325	1.48	38	50	10	5	4.8	3.6/3.4	3.7	182	1388	3.3
D22	192	15	319	1.27	40	47	11	3	4.3	0.62	3.7/3.5	3.8	147	1422	3.0	4.1	...
D23	192	30	362	1.56	31	58	12	0	4.8	10	146	...	3.1/3.0	3.0	451	459	3.7	4.1	...
D24	232	10	467	1.32	39	51	11	1	4.8	0.60	3.6/3.4	3.7	190	1136	3.2	4.0	...
D25	272	30	345	1.67	27	60	13	2	4.7	15	195	...	2.9/3.0	3.1	473	314	4.5	4.8	4 × 10 ¹²
D26	392	30	458	1.80	20	66	14	0	4.7	21	269	0.40	2.0/1.1	2.3	691	184	5.3	5.6	3 × 10 ¹¹
E1	272	5	552	1.46	38	52	10	4	4.7	359	230	3.4	4.2	...
E2	272	10	549	1.44	38	51	11	9	4.5	3.4	4.6	1 × 10 ¹⁴
E3	272	15	409	1.26	34	55	12	2	4.7	11	137	0.46	3.1/2.9	3.5	372	330	3.5	4.6	5 × 10 ¹⁴
B1	300	30	1156	1.75	24	63	13	0	4.8	13	183	...	2.5/2.0	2.6	557	233	4.3	4.5	9 × 10 ¹²
B3	400	30	721	2.13	16	68	15	0	4.5	24	311	...	2.1/1.8	2.3	695	198	6.3	6.8	1 × 10 ¹¹
B4	450	30	672	2.27	11	73	16	0	4.6	25	344	<0.3	1.7/1.0	1.8	720	172	7.1	7.6	1 × 10 ¹⁰
B6	350	30	924	1.83	19	65	16	5	4.0	19	258	<0.3	2.3/2.1	2.5	550	565	4.7	5.1	...

^aAll other growth conditions were held constant at a pressure of 200 mTorr, total flow rate of 50 sccm, partial *ortho*-carborane + argon flow rate of 0.2, and growth time of 30 min, except in the case of B1–B6, which were grown for 45 min.

^bResults were obtained by ellipsometry.

^cResults were obtained by nuclear reaction analysis (atomic percentages of B, C, and H calculated relative to total BCH composition only; atomic percentage O calculated relative to BCOH composition).

^dResults were obtained by nanoindentation.

^eResults were obtained by positron annihilation lifetime spectroscopy.

^fResults were obtained by optical absorption spectroscopy.

^gResults were obtained by capacitance–voltage measurements (Hg probe).

^hResults were obtained by current–voltage measurements (Hg probe).

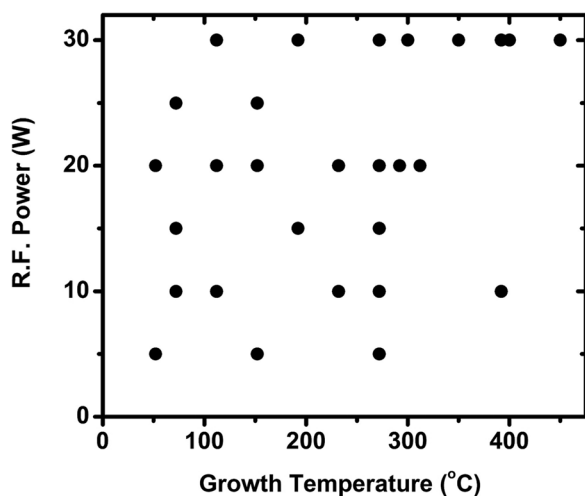


FIG. 1. Representation of parameter space covered in present study by varying growth temperature and R.F. power while holding remaining growth conditions constant.

with a total flow rate of 50 sccm and a partial precursor flow rate of 0.2—that is, 40 sccm of argon was delivered directly to the showerhead, while 10 sccm of argon was first passed through the *ortho*-carborane prior to delivery to the showerhead. Batches of a-B_xC:H_y films were grown under each set of conditions on two types of 15 × 15 mm substrates: 1–15 Ω cm p-type Si(100) and Corning soda-lime glass microscope slides. Select films for FTIR measurements were grown on Al foil. Prior to being loaded into the PECVD chamber, substrates were cleaned by sonication in acetone for 60 min, followed by immersion in a standard Piranha 2:1 H₂SO₄:H₂O₂ solution for 15 min, with subsequent rinsing using deionized water and drying using a Marangoni process.⁴⁸

The thickness and optical properties of the a-B_xC:H_y films were measured using a J.A. Woollam alpha-SE spectroscopic ellipsometer system with a 1.5–3.2 eV energy range. The CompleteEase software was used for data acquisition and analysis/model fitting. To extract thin-film thickness and optical properties, a Cauchy model with a graded layer was used to model the measured ψ - Δ trajectories,⁴⁹ which gave low mean-squared error (MSE) values (<20). The high-frequency (4.6×10^{14} Hz/1.96 eV) dielectric function, $\varepsilon = \varepsilon_1 + i\varepsilon_2$, which contains both real (ε_1) and imaginary (ε_2) components, was obtained from the measured index of refraction (n) and extinction coefficient (k) values via the relationships $\varepsilon_1 = n^2 - k^2$ and $\varepsilon_2 = 2nk$.⁵⁰

The absolute atomic concentrations in the films were determined by nuclear reaction analysis (NRA). The hydrogen content was determined by the ¹⁵N nuclear reaction method.⁵¹ Briefly, the film is bombarded with ¹⁵N⁺⁺ ions, and the number of characteristic gamma rays from the ¹⁵N + ¹H → ¹²C + ⁴He + γ -ray nuclear reaction is recorded and used to determine the H content of the film. The concentrations for the other elements (B, C, N, and O) were determined by bombarding the film with a 1.2 MeV deuteron beam and recording the number of particles from the following nuclear reactions: ¹¹B(d, α_0)⁹Be, ¹²C(d, p_0)¹³C, ¹⁴N(d, α_1)¹²C, and ¹⁶O(d, α_0)¹⁴N.^{52,53} Having determined the H, B, C, N, and O concentrations, the resulting composition

was used to generate a RUMP simulation of the 2 MeV Rutherford backscattering spectroscopy (RBS) spectrum, which was compared to the measured spectrum. Comparison of the absolute RBS simulation with the measured RBS spectrum provides a powerful check that there are no major errors in the composition. Film densities were determined by multiplying the elemental concentrations by the masses of these elements and summing over all elements present to yield the areal density in g/cm², which was then divided by the film thickness (measured by ellipsometry) to yield density in g/cm³.

The indentation modulus and hardness (H) of the films were determined using nanoindentation techniques.^{53,54} The indentation load–displacement curves were measured using a Hysitron TriboIndenter equipped with a Berkovich diamond tip. A linear projection of the apparent modulus and hardness at different indentation depths to vanishing depth was used in this study to correct for substrate effects.⁵⁵ Calibration of the area function of the indenter tip and the machine compliance was performed on a fused silica specimen according to standard procedure. For statistical purposes, at least nine repeat measurements were made for each sample.

Values for thin-film pore diameter/volume were determined using positron annihilation lifetime spectroscopy (PALS). The pore diameter of amorphous films can be obtained from the relationship of antimatter (positronium, Ps) lifetime and the presence of voids, cracks, and pores present in the amorphous network. The PALS beam was run on a subset of samples at a beam energy of 3.2 keV. At this energy, most of the incident positrons stop at the film without penetrating into the substrate. The overall measure of relative porosity was calculated using the product $I \times V_{\text{sphere}}$, where I is the intensity of the Ps signal and V is the specific pore volume calculated using a spherical model pore. The specific pore volume was determined from the Ps lifetime to pore diameter conversion.⁵⁶

Attenuated total reflection Fourier transform infrared (ATR-FTIR) spectra were acquired using a Thermo Scientific Nicolet iS10 spectrometer. All spectra were collected at room temperature in reflectance mode with a germanium crystal for a-B_xC:H_y samples on aluminum foil, which contributes negligible background.

The absorption coefficients (α) for the a-B_xC:H_y films were obtained from ultraviolet–visible (UV–vis) transmission spectroscopy measurements for thin films on glass substrates (transparent from 1.5 to 4 eV). The absorption coefficient as a function of energy was obtained from the Beer–Lambert law for solid films,⁵⁷ $T = I/I_0 = \exp(-\alpha d)$, neglecting a correction for front or back surface reflection, where T is transmission, I is intensity of transmitted radiation, I_0 is intensity of incident radiation, and d is film thickness. From the absorption coefficient data, the Tauc optical band gap (E_{Tauc}) and slope parameter ($B^{1/n}$) were determined using a Tauc analysis⁵⁸ in the high-absorption-coefficient region ($\alpha \approx 10^4$ – 10^5 cm⁻¹) based on the relationship $(\alpha \cdot E)^n = B(E - E_{\text{Tauc}})$, with $n = 2$ and 3. The isoabsorption gap, E_{04} , was also determined as the energy at which α reaches 1×10^4 cm⁻¹.⁵⁹ The Urbach energy, E_U , was determined from the absorption coefficient data extracted in the exponential low-absorption-coefficient

region ($\alpha \approx \leq 10^3 \text{ cm}^{-1}$) by fitting the data to the expression $\alpha(E) = \alpha_0 \exp(-E/E_U)$.^{60,61}

Electrical measurements were done on metal–insulator–semiconductor (MIS) heterostructures, using an MDC mercury probe and controller station with a-B_xC:H_y/Si (p-type) samples. The low-frequency (total) dielectric constant, κ , was determined from thin-film capacitance measurements obtained at 100 kHz using a Keithley 590 CV analyzer. Dielectric constant values were calculated with the parallel-plate capacitor formula, defined for an MIS geometry in the accumulation region by $\kappa = Cd/\epsilon_0 A$, where C is measured capacitance, d is sample thickness, ϵ_0 is the permittivity of free space, and A is the Hg contact area. The current density (J) as a function of electric field (E) was measured using a Keithley 2400 source meter (voltage source) and a Keithley 6485 picoammeter (current sensor). The resistivity (ρ) was extracted in the linear ohmic region (typically between 0 and 10 V) of the MIS J - E curves via Ohm's law, $\rho = E/J$.

III. RESULTS

Growth conditions and properties for the series of a-B_xC:H_y films spanning PECVD parameter space in the temperature range of 50–450 °C and R.F. power range of 5–30 W are summarized in Table I. For each of the properties, a response surface^{62,63} curve was generated, and a Kriging metamodel^{64,65} was used as a qualitative tool to fit and visualize the surface.

A. Atomic composition and mechanical properties

We have analyzed the effect of growth conditions on thin-film chemical composition and mechanical properties

based on response surface curves for a-B_xC:H_y atomic concentration, density, hardness, and Young's modulus (Fig. 2). The boron-to-carbon ratio (B/C) ranges from 3.5 to 5 (representing a stoichiometry range of B_{3.5}C to B₅C) and is primarily dependent on growth temperature, increasing from ~ 3.5 at ~ 50 °C to ~ 5 at ~ 250 °C, before decreasing again to ~ 4.5 at ~ 450 °C [Fig. 2(a)]. The atomic concentration of oxygen (at. % O) in these films remains relatively low, ranging from $\sim 10\%$ in the low temperature/power regime to $< 1\%$ (below the limits of the NRA measurements) in the high temperature/power regime [Fig. 2(b)]. The atomic concentration of hydrogen (at. % H) ranges from $\sim 10\%$ to 45% and appears to be correlated nearly equally with both temperature and power, being at a maximum in the low temperature/power regime and at a minimum in the high temperature/power regime [Fig. 2(c)]. Thin-film density ranges widely, from 0.9 to 2.3 g/cm³, with a response surface following a near inverse trend to that for at. % H [Fig. 2(d)].

A subset of predominantly low-density films was selected for PALS analysis to investigate porosity. Films with densities in the range of 0.9–1.8 g/cm³ exhibited pore sizes ranging from 0.69 to 0.40 (± 0.02) nm in diameter and Ps intensities from 10% to 1.5%, yielding IV values of relative porosity that nominally correlate with film density (see supplementary material for IV vs density data⁶⁶). Moreover, no pore interconnection was observed for even the most porous films. A few higher density samples (1.8–2.3 g/cm³) did not present any discernible pores, which suggests that they have pore sizes ≤ 0.3 nm since this represents the limit of the PALS analysis.⁵⁶ The hardness (H) and Young's modulus (E) response surface curves [Figs. 2(e) and 2(f)] trend as a function of growth temperature and power similarly to

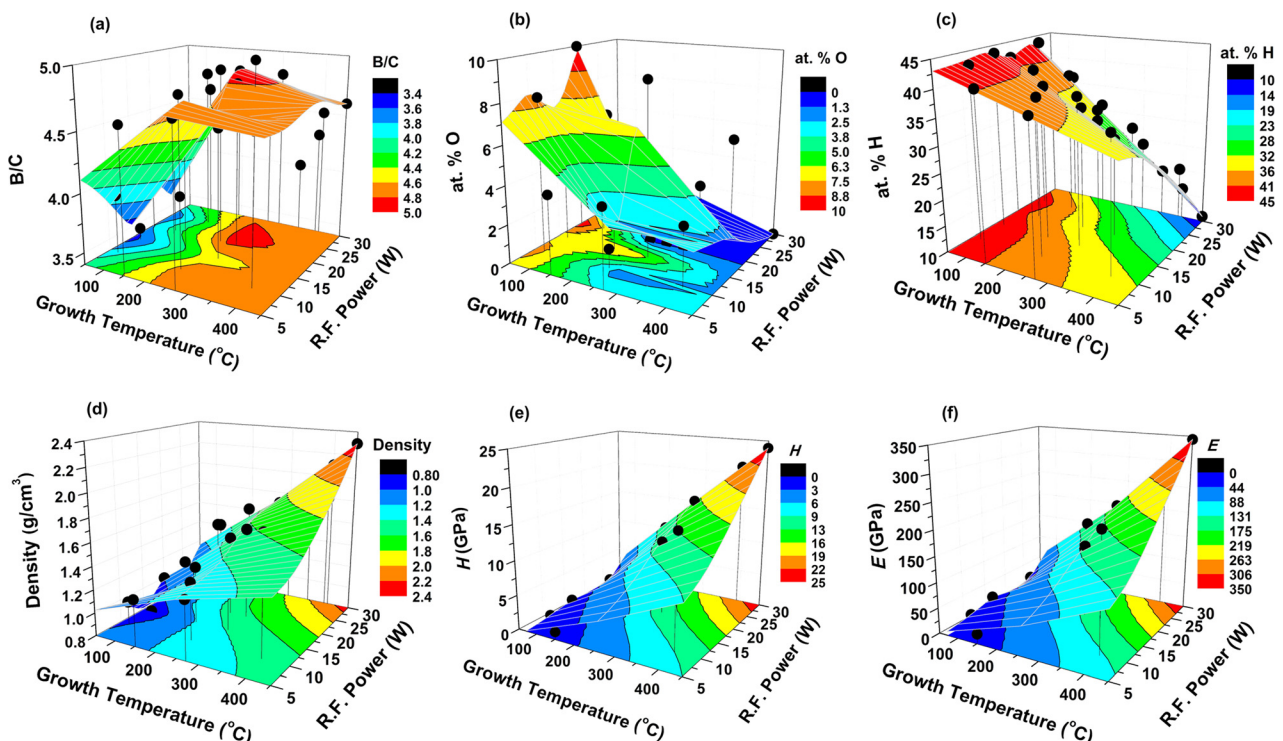


FIG. 2. Growth temperature/power response surface curves for: (a) B/C ratio, (b) at. % O, (c) at. % H, (d) density, (e) hardness, and (f) Young's modulus. The black circles represent actual data points and the colored surfaces the Kriging metamodel fit.

density. At low densities ($<1.2 \text{ g/cm}^3$), hardness ranges from 1 to 2 GPa and Young's modulus from 10 to 30 GPa, whereas for higher densities in the range of 1.3 to 2.3 g/cm^3 , hardness ranges from 5 to 25 GPa and Young's modulus from 100 to 350 GPa.

Chemical bonding information was obtained from FTIR spectroscopy. The spectra of representative high-density (2.3 g/cm^3) and low-density (0.9 g/cm^3) films, with corresponding stoichiometries of $\text{a-B}_{4.6}\text{C:H}_{0.7}$ and $\text{a-B}_{3.5}\text{CO}_{0.5}\text{H}_{3.5}$, respectively, are given in Fig. 3 along with the spectrum of the *ortho*-carborane precursor. We note that the intensities are not calibrated, and therefore spectra can only be compared qualitatively and not quantitatively. The $\text{a-B}_x\text{C:H}_y$ spectra exhibit similar features to those previously reported for other a-BC:H films.^{44,67–69} A peak at $3060\text{--}3070 \text{ cm}^{-1}$ is attributed to an intra-icosahedral C–H stretching mode, and a peak at 2560 cm^{-1} to an intra-icosahedral B–H stretching mode.⁷⁰ Both of these peaks are also present in the *ortho*-carborane spectrum,⁷¹ which reinforces their assignment. The intensity of the B–H stretch confirms that there is a significant amount of hydrogenation of the carborane units in the $\text{a-B}_x\text{C:H}_y$ films. A number of weak peaks are also observed in the region associated with sp^3 hydrocarbon C–H stretching modes ($2800\text{--}3000 \text{ cm}^{-1}$). Clear peak maxima at $\sim 2920 \text{ cm}^{-1}$ and $\sim 2850 \text{ cm}^{-1}$ can be assigned to sp^3 CH_2 asymmetric and symmetric stretching modes.^{72,73} Their presence is consistent with the proposed existence of bridging CH_2 -based hydrocarbon groups.⁷⁴ Any differences between the spectra for the low- and high-density films in this region are very subtle, and we cannot confidently make additional assignments (e.g., the identification of CH_3 groups) or quantitative determinations

without additional information. One feature that has been observed in spectra of a-B:H and a-BC:H is a very broad peak at $\sim 2000 \text{ cm}^{-1}$ assigned to a bridging B–H–B configuration,^{68,70} but this is not observed here. A peak at $\sim 1600 \text{ cm}^{-1}$ is typically assigned to the three-center C–B–C chain in crystalline boron carbide;⁷⁵ however, it is not clear that this feature should be present in the amorphous solid, and the identity of this peak remains ambiguous. Peaks below 1100 cm^{-1} are assigned to icosahedral vibrational modes.⁷¹ The most distinct difference in this region for the two $\text{a-B}_x\text{C:H}_y$ films is the presence of a strong peak at 820 cm^{-1} in the low density films, which we cannot definitively assign. A strong peak at 3200 cm^{-1} observed for the low-density film is assigned to an O–H stretching vibration and is consistent with the incorporation of some oxygen. It is plausible that a majority of this O–H is in the form of boric acid, as we also observe a very strong peak at 1410 cm^{-1} and a second strong sharper peak at 1200 cm^{-1} for this same sample that can be assigned to this impurity.^{76,77} A strong, broad peak between 1100 and 1300 cm^{-1} often dominates a-BC:H spectra, although its energy and assignment vary. Shirai *et al.* have proposed that a peak at $\sim 1100 \text{ cm}^{-1}$ is due to a B–C stretch, specifically involving extra-icosahedral C as a network modifier.⁷⁸ However, this is not consistent with the assignment by Lin and Feldman of a peak at $\sim 1280 \text{ cm}^{-1}$ as an icosahedron-based mode⁷⁹ nor of the typical assignment of this peak in crystalline boron carbide.⁷⁵ Some of the most diagnostic hydrocarbon-based features can be found in the $1300\text{--}1500 \text{ cm}^{-1}$ region, such as methyl or methylene bending modes.^{73,80–82} However, while some of these features may be observed (e.g., a distinct peak at 1315 cm^{-1} may be indicative of a CH_2 bending or C–C stretching mode), because of the number of overlapping peaks in this region and the interference due to strong boric acid peaks, it is difficult to make any definitive assignments or comparisons between the carbon-rich and carbon-poor films. While the FTIR analysis cannot provide an extremely detailed picture of the local physical structure of $\text{a-B}_x\text{C:H}_y$, it is generally consistent with our previous analysis based on solid-state nuclear magnetic resonance (SS-NMR) spectroscopy. These results suggested that $\text{a-B}_x\text{C:H}_y$ can be considered as “polymeric *o*-carborane,” and consists of partially hydrogenated partially cross-linked $\text{C}_2\text{B}_{10}\text{H}_{12}$ icosahedral units and bridging hydrocarbon chains.⁷⁴ A more thorough understanding of the structural details will require a deeper level of analysis, which is beyond the scope of this work.

In sum, varying growth temperature and R.F. power gives rise to a range of $\text{a-B}_x\text{C:H}_y$ variants with significant differences in chemical composition and mechanical properties. In the low temperature/power growth regime, we obtain (relatively) soft, low-density films that are both hydrogen and carbon rich with approximate stoichiometry of $\text{a-B}_{3.5}\text{C:H}_3$, whereas in the high temperature/power regime, we obtain hard, high-density films with lower carbon content and significantly lower hydrogen content with approximate stoichiometry of $\text{a-B}_{4.5}\text{C:H}$. In Fig. 4, we provide hypothetical models to represent these two extremes based on structural information from FTIR and SS-NMR spectroscopy. These models are purely illustrative and were generated by condensing a

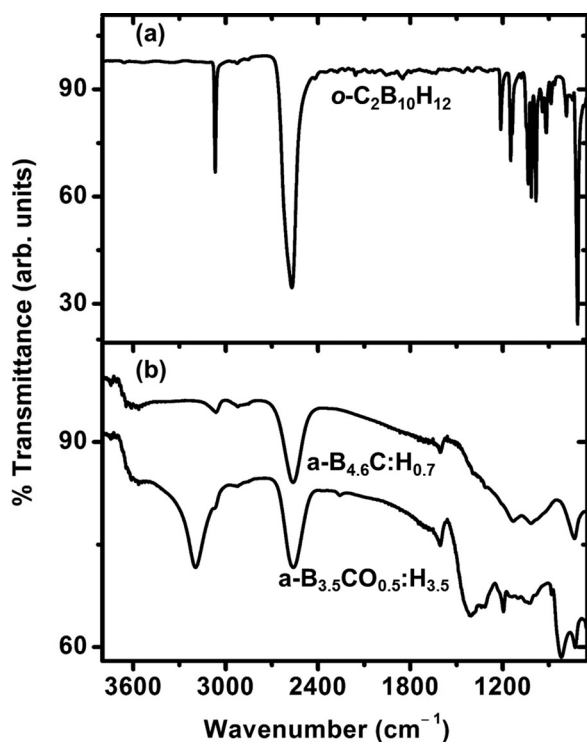


FIG. 3. FTIR spectra for (a) *ortho*-carborane and (b) representative high-density (B4, 2.3 g/cm^3 , $\text{a-B}_{4.6}\text{C:H}_{0.7}$) and low-density (D18, 0.9 g/cm^3 , $\text{a-B}_{3.5}\text{CO}_{0.5}\text{H}_{3.5}$) films.

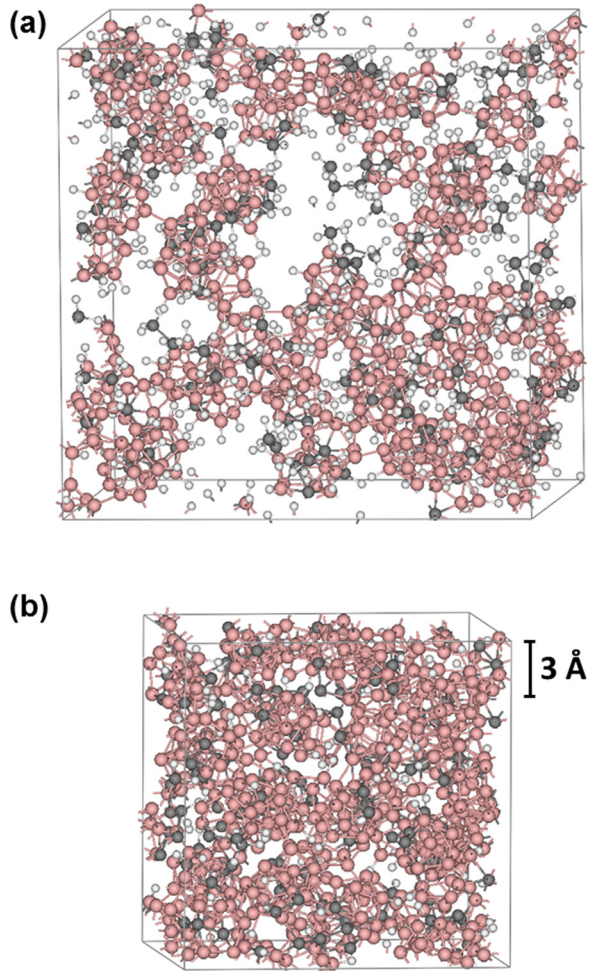


FIG. 4. Hypothetical models illustrating the local physical structure of amorphous hydrogenated boron carbide (boron = pink, carbon = gray, and hydrogen = white) in different density extremes: (a) low-density (0.9 g/cm^3) films with approximate stoichiometry of $\text{a-B}_{3.5}\text{C:H}_3$ and pores with diameters on the order of 0.7 nm (compare to D18/D19), and (b) high-density (2.4 g/cm^3) non-porous films with stoichiometry of $\text{a-B}_{4.5}\text{C:H}$ (compare to B4).

hypothesized set of chemical fragments into a simulation cell to produce a model with a given thin-film density and stoichiometry.

B. Electronic and optical properties

Optical absorption spectroscopy is a particularly useful technique for investigating the electronic structure and disorder in amorphous solids. In an amorphous solid, disorder-induced localized states give rise to exponential band tails known as Urbach tails. The point at which extended or delocalized band states give way to localized states is defined as the mobility edge, and the separation between mobility edges for the valence band (VB) and conduction band (CB) defines the mobility gap, analogous to the band gap, E_g , in crystalline solids. The absorption spectrum in amorphous solids can thus be represented by a superposition of optical transitions occurring between combinations of extended states, localized states, and mid-gap states.^{45,58} Transitions occurring from extended VB to extended CB states define the high-energy high-absorption-coefficient region of the α vs E spectrum, from which we can obtain optical band gap information.

Tauc showed that this region of the spectrum can be modeled by a power law according to $\alpha = B(E - E_g)^n/E$,⁵⁸ which can be rearranged to $(\alpha \cdot E)^{1/2} = B^{1/2}(E - E_{\text{Tauc}})$ (n is typically defined as 2 for amorphous solids), such that the Tauc optical band gap, E_{Tauc} , and the Tauc parameter, $B^{1/2}$, can be extracted from a plot of $(\alpha \cdot E)^{1/2}$ vs E as the intercept and slope of the linear region, respectively. Other methods have been employed to determine the optical band gap of amorphous solids,⁵⁹ including the isoabsorption method,^{59,61,83} where a gap is empirically defined at a given absorption coefficient value (typically E_{04} at $1 \times 10^4 \text{ cm}^{-1}$), as well as the use of alternative values for “ n ” in the Tauc equation (typically 3, as may be appropriate for boron-rich solids^{84,85}). The accuracy of these methods depends on the specific form of the density of states in a given material and other factors beyond the scope of this paper. Transitions involving localized states contribute to the exponential lower-energy lower-absorption-coefficient region of the α vs E spectrum. Specifically, the exponential edge of the absorption curve has been shown to be primarily defined by transitions between localized VB states and extended CB states. This region of the curve can be modeled by $\alpha(E) = \alpha_0 \exp(-E/E_U)$, where the decay factor, known as the Urbach energy (E_U), is primarily a measure of the width of the valence band tail,⁶¹ and can be obtained as the slope of the curve for a plot of $\ln(\alpha)$ vs $\ln(E)$ [i.e., $E_U = d\ln(\alpha)/d\ln(E)$]. Both the Urbach energy and the Tauc slope parameter, $B^{1/2}$, provide some measure of disorder in a solid; however, they do not necessarily probe the same type(s) of disorder nor do they have the same meaning in all materials.^{60,86}

We have extracted optical band gap values for $\text{a-B}_x\text{C:H}_y$ using the Tauc method ($n = 2$ and 3) as well as the isoabsorption method (E_{04}), and the results are summarized in Table I. Representative absorption coefficient spectra for a subset of $\text{a-B}_x\text{C:H}_y$ films with annotated E_{04} values and their corresponding Tauc plots ($n = 2$) are shown in Fig. 5. Both Tauc analyses ($n = 2$ and 3) yielded similarly linear fits ($R^2 = 0.99$), but the E_{Tauc} values extracted using $n = 3$ were systematically lower than those using $n = 2$ by an average of 0.4 eV . In contrast, the E_{04} method yielded band gap values systematically higher than those obtained by a Tauc analysis with $n = 2$ by an average of 0.3 eV [Fig. 6(a)]. In addition to the band gap values, we also obtained $B^{1/2}$ values from the Tauc analysis ($n = 2$) as well as Urbach energy values using an exponential fitting of the absorption coefficient curves in the appropriate region.

Figs. 7(a)–7(c) display the response surfaces for Tauc band gap, Tauc slope parameter (in the form of $B^{1/2}$), and Urbach energy. The optical band gap ranges from 3.8 to 1.7 eV and $B^{1/2}$ from 1650 to $170 \text{ eV}^{-1/2} \text{ cm}^{-1/2}$, both decreasing as a function of temperature and power, while the Urbach energy exhibits the opposite behavior, increasing from 0.1 to 0.7 eV . All three of the parameters are clearly correlated, as can be seen from Fig. 6. The optical band gap range measured here is consistent with previous reports for *ortho*-carborane-based $\text{a-B}_x\text{C:H}_y$ films, for which E_g values have been cited between 1.5 (Ref. 87) and 3.8 eV .⁸⁸ The Tauc slope parameter has been previously reported for $\text{a-B}_4\text{C}$ as $529 \text{ cm}^{-1/2} \text{ eV}^{-1/2}$,⁸⁴ which is within the same

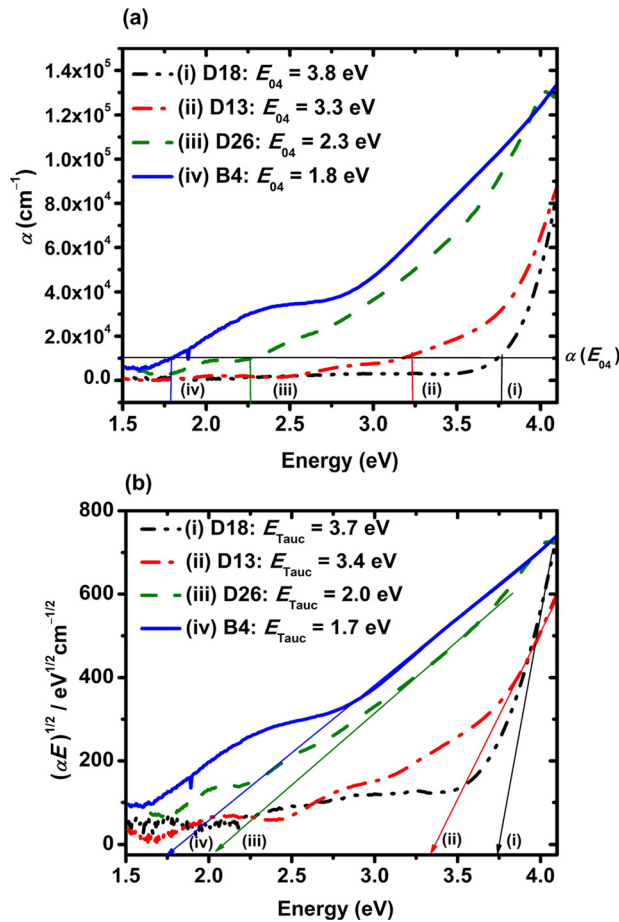


FIG. 5. Representative absorption coefficient curves (a) and corresponding Tauc plots ($n=2$) (b) for a subset of $a\text{-B}_x\text{C:H}_y$ samples of varying density and band gap illustrating extraction of E_{04} and E_{Tauc} values. The oscillations evident in the spectra are a result of thin-film optical interference.

range as for the films characterized here. The Tauc slope parameter for $a\text{-B}_x\text{C:H}_y$ is further comparable to those found in $a\text{-Si:H}$,^{86,89,90} $a\text{-Ge:H}$,^{86,91} and $a\text{-SiC:H}$,^{92,93} which range anywhere from 100 to $1200 \text{ cm}^{-1/2} \text{ eV}^{-1/2}$. The authors are not aware of any reports of E_U values for B_xC or $a\text{-B}_x\text{C:H}_y$ films. The Urbach energy range for $a\text{-B}_x\text{C:H}_y$ (0.1–0.7 eV) is much higher than that found in $a\text{-Si:H}$ (0.05–0.1 eV)⁶⁰ as well as the vast majority of amorphous solids,⁹⁴ although it is closer to that of $a\text{-C:H}$ ⁹⁵ or organic polymers,⁹⁴ which is on the order of hundreds of meV.

The relative permittivity, ϵ_r , of a solid is a complex frequency/energy-dependent quantity that represents the sum of orientation polarization (movement of permanent dipoles), distortion polarization (vibration of polar bonds), and electronic polarization (displacement of electron cloud) contributions to the total polarization response to an electric field.⁹⁶ The macroscopic relative permittivity of a material can be related to the microscopic properties of the individual molecular constituents by the Debye equation, $(\epsilon_r - 1)/(\epsilon_r + 2) = [N(\alpha_e + \alpha_d + \mu^2/3k_B T)]/3\epsilon_0$, where N is the molecular density, the α_e and α_d terms represent the electronic and distortion polarization contributions in the molecules, respectively, and the μ^2 term takes into account the permanent dipole moments that give rise to the orientation polarization contribution ($k_B =$ Boltzmann constant,

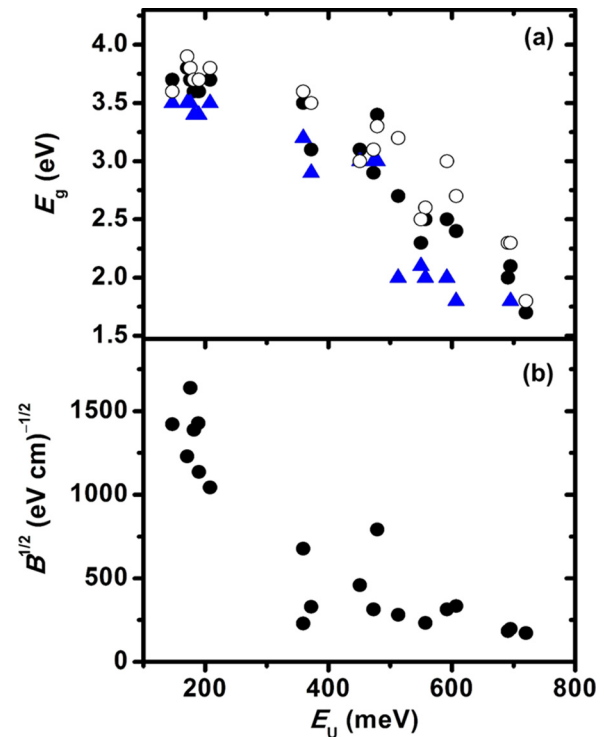


FIG. 6. Correlations between (a) band gap values, E_{Tauc} [$n=2$ (●) and $n=3$ (▲)] and E_{04} (○), and Urbach energy and (b) Tauc slope parameter, $B^{1/2}$, and Urbach energy, for $a\text{-B}_x\text{C:H}_y$ films.

$T =$ temperature, and $\epsilon_0 =$ permittivity of free space).⁹⁶ At high (optical) frequencies, only α_e contributes, at moderate (infrared) frequencies, we probe the sum of α_e and α_d contributions, and at low (microwave/radio) frequencies, all polarization contributions are at play. For our purposes, we take the total dielectric constant, κ , which represents the sum of all polarization contributions, as the relative permittivity measured at 100 kHz, and the electronic contribution to the dielectric constant, ϵ_1 , as the real part of the relative permittivity measured at high frequency (4.6×10^{14} Hz). The difference between the two terms, $\kappa - \epsilon_1$, therefore represents the combined orientation and distortion polarization contributions.

The response surfaces for the total dielectric constant, the electronic contribution to the dielectric constant, and the difference between the two ($\kappa - \epsilon_1$) for the series of $a\text{-B}_x\text{C:H}_y$ films are given in Figs. 7(d)–7(f). The total dielectric constant ranges from 3.1 to 7.6, with the electronic contribution ranging from 2.3 to 7.1, both increasing with higher growth temperature and power. Because $a\text{-B}_x\text{C:H}_y$ contains very low- Z atomic constituents (B, C, and H), which implies a low mass and electron density, we expect ϵ_1 to be low, which is found to be the case here. The range of ϵ_1 values observed is also consistent with those previously found in PECVD $a\text{-B}_x\text{C:H}_y$ films, wherein ϵ_1 values of $\sim 2\text{--}4$ were observed,^{35,49} and in higher density crystalline B_xC , wherein ϵ_1 values of ~ 7 were measured.⁹⁷ Further, because $a\text{-B}_x\text{C:H}_y$ contains only low polarity bonds (B–B, B–C, B–H, and C–H), which implies low distortion and orientation polarization contributions, we expect the electronic polarization contribution, ϵ_1 , to dominate κ , which is indeed observed.

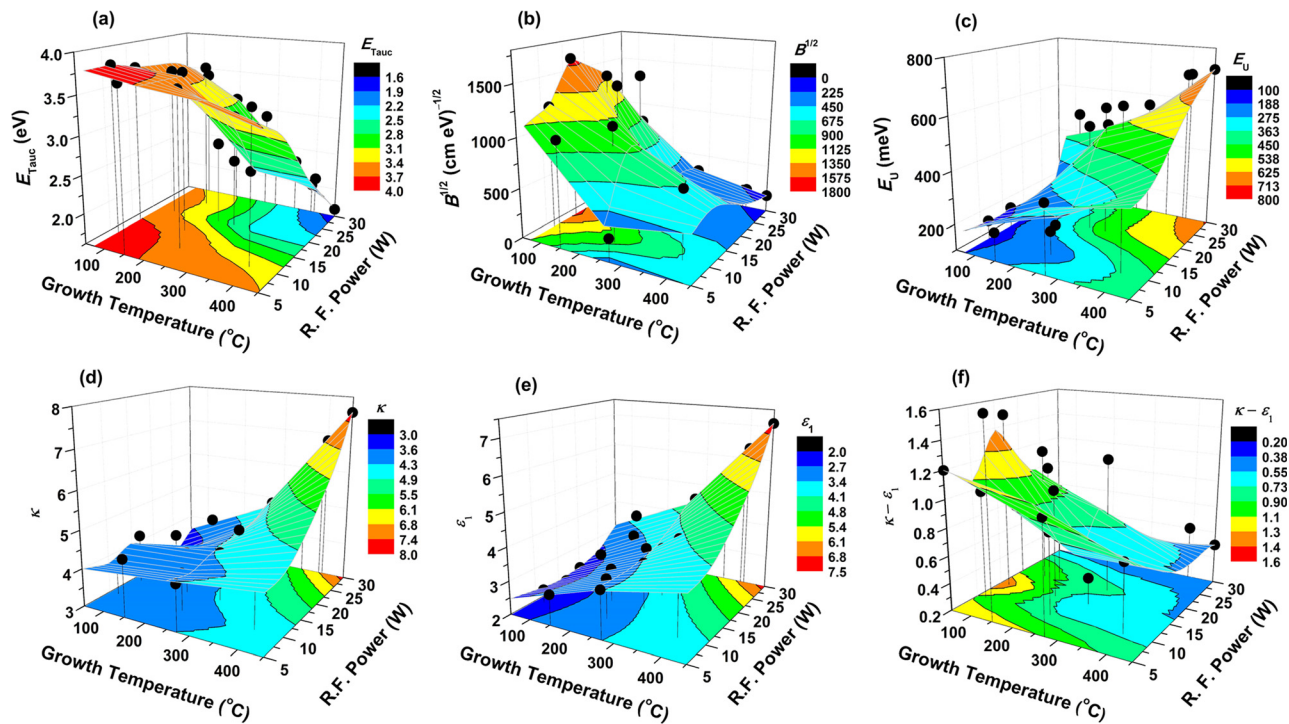


FIG. 7. Growth temperature/power response surface curves for: (a) Tauc optical band gap, E_{Tauc} ($n=2$), (b) Tauc slope parameter, $B^{1/2}$, (c) Urbach energy, E_U , (d) total dielectric constant, κ , (e) the electronic contribution to the dielectric constant, ϵ_1 , and (f) the orientation/distortion contribution to the dielectric constant, $\kappa - \epsilon_1$.

This has also been shown to be true in the case of $c\text{-B}_x\text{C}$, as demonstrated by Samara *et al.*, who reported a low distortion contribution in the range of 0–2.⁹⁷

For the $a\text{-B}_x\text{C:H}_y$ films measured, ϵ_1 makes up the majority ($\sim 60\%$ – 90%) contribution to the total κ . The difference between the two [$\kappa - \epsilon_1$, Fig. 7(f)] does not scale with ϵ_1 or κ , but rather exhibits an increase at low growth temperature and power, which results in a higher κ than might be expected in this range. If we refer back to the NRA results [Table I, Fig. 2(b)], we see that the at. % O scales closely with $\kappa - \epsilon_1$. Therefore, although films grown at low temperature and power have low densities, which should yield a low total κ , the presence of oxygen-containing functional groups with polar bonds such as B–O, and O–H is expected to lead to an increase in the distortion and potentially orientation polarization contributions, which may explain all or part of the higher $\kappa - \epsilon_1$ contribution in this growth regime.

C. Electrical transport properties

The response surface for electrical resistivity for the series of $a\text{-B}_x\text{C:H}_y$ films is shown in Fig. 8(a), from which we can see that it varies across several orders of magnitude from 10^{10} to 10^{15} Ω cm. Trends as a function of growth temperature and power are less evident than in the case of the other material properties investigated in this study. Previous resistivity measurements on carborane-based $a\text{-B}_x\text{C:H}_y$ films have been reported in the range of 10^8 – 10^{10} Ω cm,^{10,28} and therefore the films produced here are significantly more insulating. Although resistivity is a useful fundamental material property, from an application perspective, one of the key electrical properties of interest is leakage current. From

Fig. 8(b), we see that the leakage current generally trends with resistivity at a moderately low electric field of 0.5 MV/cm. At higher electric fields, the leakage current mechanism begins to diverge from ohmic transport, and therefore the direct resistivity/leakage current correlation can breakdown. A more detailed analysis of electrical properties and current–voltage behavior is beyond the scope of this paper.

IV. DISCUSSION

A. Atomic composition, physical structure, and mechanical properties

One might first consider the atomic structure of $a\text{-B}_x\text{C:H}_y$ as a base for understanding its material properties. Determining atomic structure is a particularly challenging problem in the case of $a\text{-B}_x\text{C:H}_y$ because of not only its amorphous nature but also its molecule-based constituents and the many configurations into which these can be arranged. We have previously proposed, based on solid-state nuclear magnetic resonance spectroscopy, that $a\text{-B}_x\text{C:H}_y$ consists of partially hydrogenated $\text{C}_2\text{B}_{10}\text{H}_{12}$ icosahedral units and hydrocarbon chains with varying degrees of cross-linking.⁷⁴ The FTIR results described here support these conclusions. This picture, however, remains incomplete, and additional rigorous studies will be needed to prove out this model and to fill in the missing pieces. Despite the complexity and unknowns associated with the atomic structure of $a\text{-B}_x\text{C:H}_y$, we have found that hydrogen content appears to be a relatively simple and efficient proxy for mapping thin-film properties. As seen in Fig. 9, the at. % H displays a strong correlation with a majority of the properties investigated in this study.

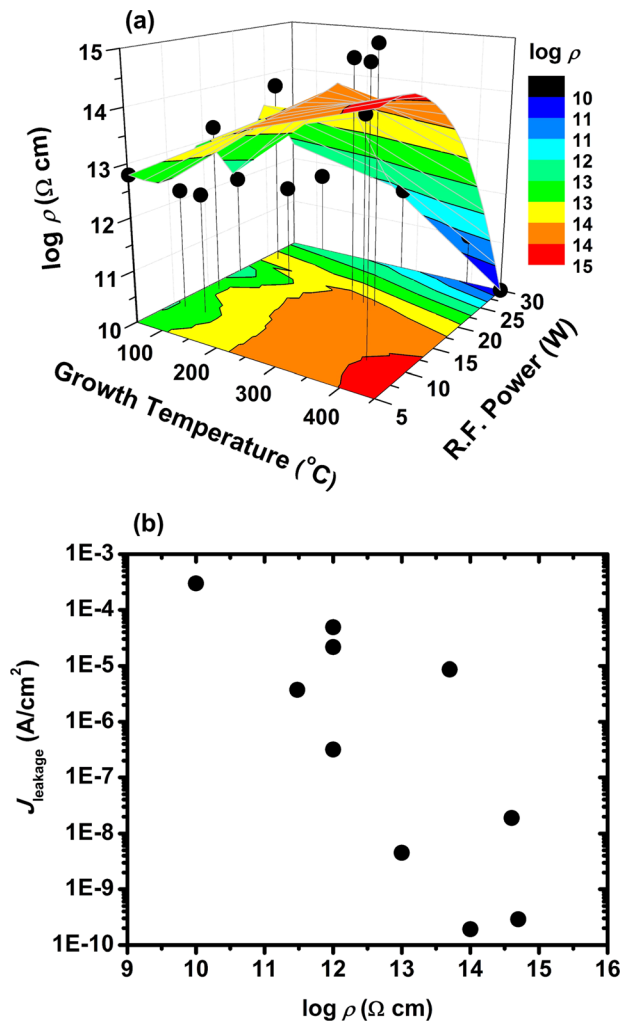


FIG. 8. (a) Growth temperature/power response surface curve for electrical resistivity and (b) correlation between leakage current density (at 0.5 MV/cm) and resistivity.

In particular, we observe a distinct inverse linear trend between hydrogen concentration and thin-film density [Fig. 9(a)], where density decreases commensurate with increasing hydrogen content. Hypothetical models of $\text{a-B}_x\text{C}_y\text{H}_z$ illustrating the hydrogen-rich/low-density and hydrogen-deficient/high-density extremes were given in Fig. 4. Density can be reduced to the atomic mass of the constituents and the relative free volume in the solid (i.e., atoms/volume). Therefore, to a first approximation, hydrogen content plays a direct role in determining thin-film density because of both its low atomic number ($Z=1$), which decreases the average atomic mass of the constituents, and its coordination number of 1, which decreases the average network coordination and consequently increases the free volume in the solid.⁹⁸ Relatively small (0.40 to 0.69 nm), isolated pores are also observed in the films, with the pore diameter appearing to trend with hydrogen content/density [Fig. 9(b)]. The increase in pore diameter observed with decreasing density represents a factor of five increase in pore volume, V .

Similar hydrogen–density trends have been observed in amorphous hydrogenated silicon (a-Si:H), wherein greater hydrogen content is correlated with lower density films. However, in a-Si:H, hydrogen atoms have been found to

reside in different chemical environments, including in vacancies as SiH groups and on the surfaces of nanovoids as SiH₂ groups. As such, the relationship between hydrogen content and density exhibits subtle variations with the hydrogen concentration regime and the microstructural features of the a-Si:H network in that regime.^{99,100} In amorphous hydrogenated carbon (a-C:H), the main structural feature controlling density is not hydrogen content *per se*, but rather sp^3/sp^2 fraction, where hydrogen tends to correlate with relative sp^3 concentration. At low hydrogen concentrations, increasing sp^3 carbon results in increasing film density due to the higher density of the sp^3 carbon network relative to the sp^2 carbon network. However, above a certain threshold, the trend reverses, and further increases in hydrogen/ sp^3 carbon are associated with a decrease in density, which can be explained by the additional sp^3 hydrocarbon groups now acting as network modifiers (terminating groups) rather than network formers, thereby increasing free volume.¹⁰¹ In a-SiC:H, hydrogen content has also been shown to correlate with density, albeit often indirectly.^{92,102–104} Similarly to a-Si:H, a-SiC:H exhibits micropores, which are associated with both SiH₂ and SiCH₃ groups to varying degrees depending on growth conditions and stoichiometric regime.¹⁰⁵ Because the hydrogen can be tied up in many ways including as SiH, SiH₂, CH₂ bridging groups, and CH₃ terminal groups, even more refinements are introduced into the density/hydrogen relationship.

Like in a-Si:H, a-C:H, and a-SiC:H, more subtle microstructural effects may also be at play for a-B_xC_yH_z, including the possibility of hydrocarbon groups acting as network modifiers vs network formers and contributing to the formation of nanopores, or incorporating in different ways in different stoichiometric regimes, or even the presence of B–H–B bridging groups,⁷⁰ often observed in a-B:H (but not here so far). However, based on the linearity of the at. % H vs density curve obtained for this set of a-B_xC_yH_z samples, we can conclude that either all of these samples fall within a single structural phase/regime or that the existence of some of these more complex structural features does not significantly skew the general trends. Overall, because hydrogen content and density are intimately related, one or both properties may be used to benchmark, and in many cases physically explain, other material properties of interest.

A strong correlation between at. % H (and consequently density) and the mechanical properties of the a-B_xC_yH_z films exists. Both hardness, H , and Young's modulus, E , increase with decreasing hydrogen content (or increasing density) [Figs. 9(c) and 9(d)]. Both properties exhibit similar behavior, where below $\sim 35\%$ H (or above densities of $\sim 1.3 \text{ g}/\text{cm}^3$), they follow a specific power law relationship, but above (below) this, the trend breaks down and a plateau is observed. Scaling relationships between Young's modulus and density of the form $E \propto D^n$, where n is a scaling exponent, have been recognized in many material systems.^{106,107} The plateau can be explained by rigidity percolation theory, which predicts that below a critical density or degree of network coordination, the number of degrees of freedom becomes equal to the number of constraints, whereupon a fundamental change in the rigidity of the solid occurs.^{108–110}

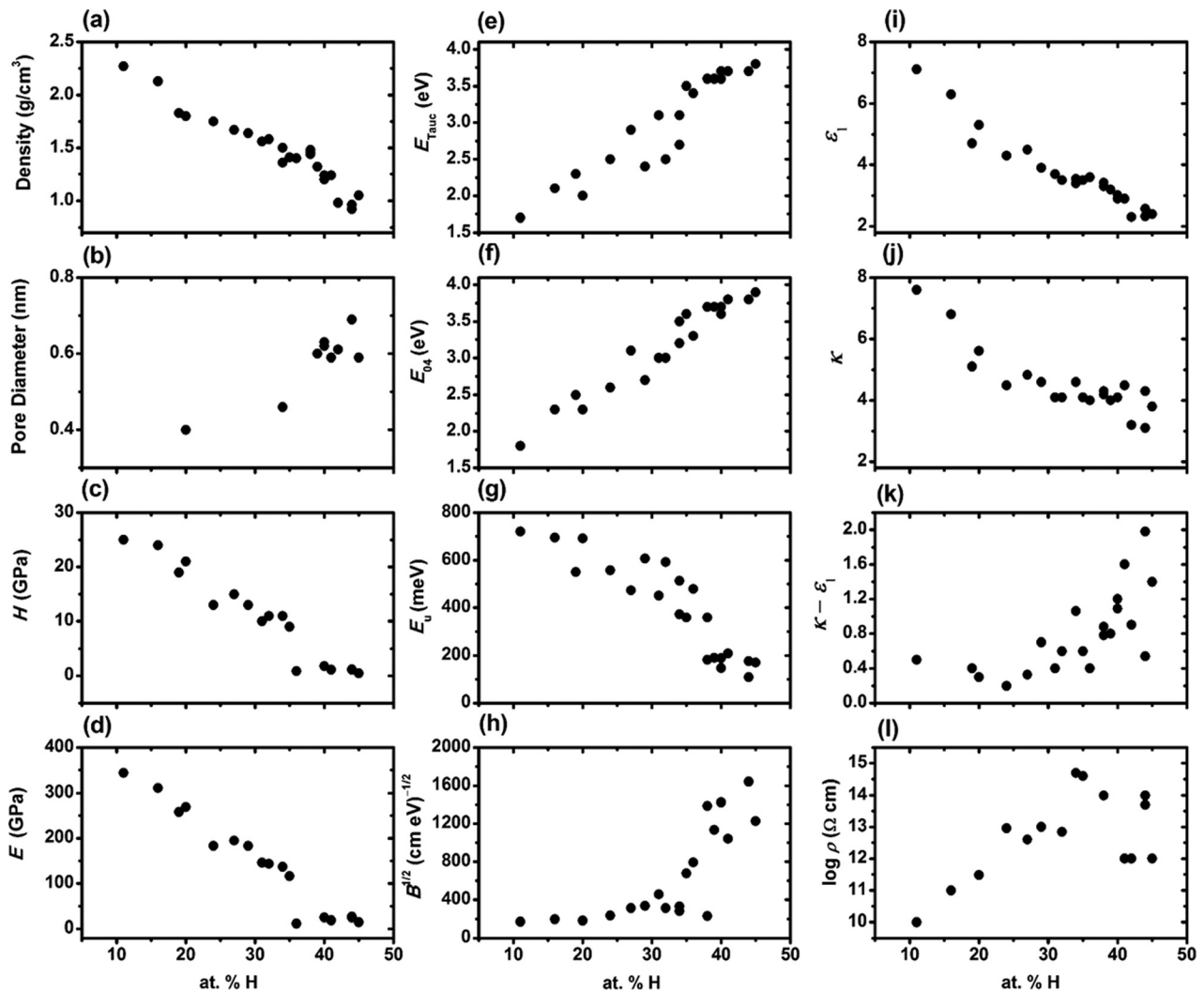


FIG. 9. Correlations between a series of material properties and atomic concentration hydrogen in $a\text{-B}_x\text{C:H}_y$ films: (a) density, (b) pore diameter, (c) hardness, (d) Young's modulus, (e) Tauc optical band gap ($n=2$), (f) E_{04} optical band gap, (g) Urbach energy, (h) Tauc slope parameter ($n=2$), (i) high-frequency dielectric constant, (j) total (low-frequency) dielectric constant, (k) $\kappa - \epsilon_1$, and (l) electrical resistivity.

B. Electronic and optical properties

Hydrogen content and density are also clearly correlated with the electronic structure of $a\text{-B}_x\text{C:H}_y$. As these films become more hydrogen rich and less dense, the optical band gap [Tauc ($n=2$) and E_{04} , shown in Figs. 9(e) and 9(f), respectively] and Tauc slope parameter [$B^{1/2}$, Fig. 9(h)] increase, while the Urbach energy decreases [Fig. 9(g)]. The band gap (Tauc/ E_{04}) increases linearly from 1.7 eV to 3.8 eV as a function of increasing hydrogen content. The same general correlation between hydrogen concentration and band gap is observed in $a\text{-Si:H}$,^{60,90} $a\text{-C:H}$,¹⁰¹ and $a\text{-SiC:H}$,¹⁰² however, as we will discuss below, the mechanisms differ. In $a\text{-B}_x\text{C:H}_y$, the Urbach energy decreases linearly from 0.7 to 0.1 eV as a function of increasing hydrogen concentration. A decrease in Urbach energy with increasing hydrogen concentration is also observed in $a\text{-Si:H}$,⁶⁰ although the opposite trend is observed in $a\text{-SiC:H}$ ¹⁰² and $a\text{-C:H}$.^{94,95} Lastly, the $B^{1/2}$ parameter increases with hydrogen content from ~ 200 to $1600 \text{ eV}^{-1/2} \text{ cm}^{-1/2}$, however the relationship is not linear as in the case of E_g and E_U .

A number of theoretical and empirical models exist that relate band gap to fundamental material properties. From a chemical bonding point of view, as two atoms are brought together, bonding and antibonding molecular orbitals (MOs) are formed, creating an energy gap between the highest occupied and lowest unoccupied frontier MOs. As additional atoms are brought together to form an extended solid, the discrete MO energy levels broaden into bands, effectively decreasing the gap between band edges.¹¹¹ The same reasoning applies to molecule-based solids, where in a polymeric material, for example, the band gap decreases with increasing chain length as a greater number of monomers are bonded together. In a hydrogenated amorphous solid, the role of hydrogen—because it is one-fold-coordinate in the vast majority of circumstances—is inevitably to decrease the average coordination number of the network¹¹² (see, for example, the direct correlation between coordination number and at. % H in $a\text{-SiC:H}$ ¹⁰⁴), unless dealing with an under-coordinated network.¹¹³ Therefore, from the point of view of this simple bonding model, a decrease in hydrogen concentration and increase in density in $a\text{-B}_x\text{C:H}_y$, commensurate

with greater connectivity in the solid (i.e., a higher average coordination number, or increased cross-linking between icosahedral “monomer” units), would imply a lower band gap.

The factors contributing to band gap can be more complex, however, as exemplified by the case of amorphous hydrogenated silicon. Pastawski *et al.* attributed the increase in band gap with hydrogen content to a decrease in silicon coordination number,¹¹⁴ which is the same explanation that we provide above for a-B_xC:H_y. Papaconstantopoulos and Economou, however, discussed the widening of the gap in terms of local chemical environment and its effect on valence/conduction band character (rather than merely the energy between the two).¹¹⁵ Cody *et al.* argued that the band gap was actually related to disorder and only indirectly to hydrogen content, with greater disorder being correlated with a decreased band gap.⁶⁰ Mahan *et al.* have explored how different types of disorder in a-Si:H can individually influence E_g ,¹¹⁶ while Legesse *et al.* showed that different trends in E_g exist for different hydrogen concentration regimes,¹¹⁷ which helps to rectify some of the differing interpretations. In all likelihood, most or all of these explanations hold some degree of validity. In amorphous hydrogenated carbon, again, we see different effects at play. In a-C:H, the band gap is defined by the sp²-based π orbitals. Band gap is strongly correlated to sp²/sp³ fraction and, importantly, to the actual configuration of the sp² carbon. Thus, any correlation with hydrogen is indirect.^{72,73} In a-SiC:H, band gap is usually reported as a function of carbon fraction, where it widens with increasing C up to a certain point (although, as Solomon notes, the properties of the samples depend strongly upon growth conditions and trends become lost when data from different experiments are compared¹¹⁸). This increase in band gap is typically explained as the replacement of Si–Si bonds by stronger Si–C bonds, which results in a lowering of the valence band edge and increase in band gap.^{102,119–121} It has also been proposed that hydrogenation additionally contributes to the widening of the gap, albeit to a lesser degree.^{119,120}

Although we propose that, in a-B_xC:H_y, an increase in hydrogen concentration (and decrease in density) leads to a higher band gap because of the decrease in network connectivity/average coordination number, we do not neglect other possible contributions including the influence of specific types of disorder or the change in valence/conduction band character due either directly to hydrogen bonding or indirectly to other simultaneous changes occurring in the solid (e.g., changes in hydrocarbon content and type). Additional studies of the density of states and of the disorder, both experimental and theoretical, will be needed to more conclusively address this issue.

As mentioned previously, both the Urbach energy and Tauc parameter are considered measures of disorder in amorphous solids. Disorder can come in a number of flavors, including thermal disorder (vibrational/dynamic), structural disorder (deviation of atoms away from a perfectly ordered lattice, manifest in the form of a variation in bond lengths and angles), topological disorder (variation in structural features at a medium-range length scale, such as chain size,

cluster size, and ring size distributions), and substitutional disorder (substitution of one type of atom for another, including voids and dangling bonds). In a-Si:H, the Urbach energy—defined in this material by the width of the valence band exponential tail—is attributed predominantly to structural disorder.^{60,86} An inverse relationship between hydrogen concentration and Urbach energy is observed, which has been explained in terms of the ability of hydrogen to release strain in the amorphous network, thereby leading to a decrease in structural disorder and increase in E_U . The same holds in the case of a-Ge:H.¹²²

The meaning of the Urbach energy, and its potential correlation with hydrogenation, is not universal, however. In a-C:H, the relationship between hydrogen concentration and Urbach energy is opposite to that in a-Si:H, and the origin of E_U both more complex and more controversial. Robertson states that, similarly to the relationship between band gap and sp² clustering, the Urbach energy is specifically related to the topological disorder arising from variations in cluster sizes rather than structural disorder.⁷³ Fanchini and Tagliaferro, on the other hand, maintain that E_U is not related to disorder, but rather to the Gaussian width of the π band; however, this conclusion is based on phenomenological modeling only.⁹⁵ Casiraghi *et al.*¹⁰¹ show rather compellingly that the Urbach energy in a-C:H is related to both structural and topological disorder at low H concentration (<25%)—the same behavior that is observed in hydrogen-free amorphous carbon¹²³—but that it is related to topological disorder alone at higher H concentration (>25%), consistent with Robertson’s claims. The H concentration itself, though, exhibits different relationships with topological and structural disorder. At low H concentration, both structural and topological disorder increase with increasing at. % H, whereas at high H concentration, topological disorder continues to increase, but structural disorder decreases. At low H concentrations, it can be said that increasing hydrogen content acts to break C–C bonds and thereby increase structural disorder, whereas at higher H concentrations, it primarily acts to release strain in the network and lower structural disorder. Therefore, even though in the high H concentration regime the same inverse correlation between structural disorder and at. % H exists in both a-C:H and a-Si:H, the relationship between E_U and at. % H is the opposite in a-C:H (positive rather than negative correlation with at. % H) because now the Urbach energy is defined by topological rather than structural disorder.

In a-SiC:H, E_U has been shown to increase with increasing C fraction (and thus indirectly with H concentration, which is typically correlated with C fraction), which is typically explained by the fact that the incorporation of C into the Si network introduces disorder by distorting bond lengths and angles.^{102,120,121} Others have argued, however, that E_U is controlled by microstructure due to alloying rather than structural or compositional disorder.¹²⁴ Even if H were to have an effect on disorder, it is difficult to determine experimentally because the effect is convoluted with the influence of C. Theoretical results are mixed, suggesting both an increase and decrease in disorder as a function of hydrogenation.^{125–127} We note that the relationship between Urbach

energy and band gap is opposite in the cases of a-SiC:H and a-Si:H, where in a-SiC:H, the two are directly correlated, but in a-Si:H, they are inversely correlated.

In a-B_xC:H_y, we see the same type of trend as in a-Si:H, with E_U decreasing with increasing H content (and increasing band gap) [Fig. 9(g)]. The simplest explanation is therefore that the incorporation of H leads to a decrease in structural disorder commensurate with the formation of a lower density, lower strain network. Further, although the a-B_xC:H_y films with greater hydrogen content are also those with greater carbon content, we do not observe an increase in E_U due to the increase in carbon (see, for example, D18 and D19), which suggests that the role of carbon incorporation in the a-B_xC:H_y network is fundamentally different than in the a-SiC:H network. In a-B_xC:H_y, presumably additional hydrocarbon is involved in cross-linking icosahedra, which may even decrease the strain in the polymer compared to direct cross-linking between icosahedra. In a-SiC:H, the addition of carbon serves as a more fundamental disruption to the base Si network. Owing to the particularly complex nature of the bonding in a-B_xC:H_y, and as evidenced by a-C:H, we must remain open to additional explanations for disorder in this material, including different behaviors in different regimes of B/C/H phase space. Even in a-Si:H and related materials, the Urbach energy can potentially be influenced by more variables than simply the structural disorder defined by bond length and angle distortions.^{61,128,129}

The Tauc parameter, $B^{1/2}$, is related to the oscillator strength of the optical transition, the deformation potential (related to the electron–phonon coupling), and the deviation of atom positions from perfect lattice coordinates, the latter originating from structural disorder (i.e., deviations in bond lengths and angles) in the case of amorphous materials.¹³⁰ Whereas E_U is often said to be related to the width of the valence band tail, the $B^{1/2}$ parameter has been said to be related to the width of the conduction band tail.¹²⁰ In contrast to the Urbach energy, the magnitude of $B^{1/2}$ is inversely proportional to disorder—that is, a lower value implies increased disorder. Although both E_U and $B^{1/2}$ can be taken as measures of disorder, they do not necessarily represent identical effects, and the precise type of disorder probed by the individual parameters is not fully understood. In many cases, the two parameters exhibit an inverse linear relationship,^{91,121} implying that they do in fact probe a similar underlying disorder feature. Zanatta *et al.*^{86,128} highlight some of the more subtle differences between the two, such as sensitivity to substitutional (electronic) disorder vs. structural disorder. In a-B_xC:H_y, E_U and $B^{1/2}$ are indeed inversely correlated and exhibit the same general trends with at. % H [Figs. 9(g) and 9(h)], however the correlation between the two is not perfectly linear [Fig. 6(b)], which suggests that they do not probe identical effects and perhaps demonstrate a more complex interrelationship than in other solids. A more detailed elucidation of the origin of the disorder parameters in a-B_xC:H_y is beyond the scope of this paper.

Both the low- and high-frequency values of the dielectric constant (κ and ϵ_1 , respectively) exhibit an inverse linear correlation with at. % H, decreasing with an increase in hydrogen concentration (or decrease in density), as seen in

Figs. 9(i) and 9(j). In the case of κ , the correlation breaks down somewhat above $\sim 30\%$ H, owing we believe to the increased oxygen content in this region and therefore inflated $\kappa - \epsilon_1$ contribution from polar oxygen-based bonds [Fig. 9(k)]. The electronic dielectric constant scales with the band gap as $\epsilon_1 = 1 + [\hbar^2 N e^2] / [m (E_g)^2]$, where N is the valence electron density, and m and e electron mass and charge, respectively.¹³¹ Therefore, not only is ϵ_1 intimately related to band gap, which—as discussed above—is influenced by the degree of network connectivity in the solid, but it is also strongly dependent on mass density (number of atoms/volume) and electron density (Z of constituent atoms).^{132,133} The decrease in ϵ_1 with increasing hydrogen concentration/decreasing density can be rationalized by the effect of hydrogen concentration on band gap, and also—more directly—by the relationship between higher hydrogen content and lower mass and electron density, which are directly proportional to ϵ_1 . The total dielectric constant encompasses ϵ_1 , and therefore is expected to trend as ϵ_1 , while also reflecting additional contributions from orientation and distortion polarization components, which are represented by the $\kappa - \epsilon_1$ term. Due to the low polarity of the bonds in a-BC:H, the $\kappa - \epsilon_1$ term is small in general, and therefore κ and ϵ_1 exhibit similar magnitude. The $\kappa - \epsilon_1$ term does show an increase with increasing hydrogen content, but we propose that the majority of this effect has to do with the incorporation of oxygen in the network, and is not necessarily related to hydrogen content *per se*. A similar decrease in dielectric constant (specifically, index of refraction, n) with hydrogen content is observed in the case of a-Si:H, which can also be explained by the significant influence of H on mass and electron density.¹³⁴ Kageyama *et al.* highlight the subtleties of the relationship between dielectric function and hydrogen in a-Si:H, and how it can be explained more precisely by looking at how hydrogen is incorporated into microvoids.¹³⁵ It is possible that similar structural subtleties are at play in a-B_xC:H_y.

C. Electrical transport properties

Hydrogen content also displays a correlation with electrical resistivity [Fig. 9(l)]. As the a-B_xC:H_y films become more hydrogen rich, ρ increases by several orders of magnitude from 10^{10} to 10^{15} $\Omega\cdot\text{cm}$ in the range of 10% to $\sim 35\%$ H, at which point the data becomes scattered, and perhaps begins to decrease. To interpret this result, we can consider two different charge transport mechanisms that might occur in an amorphous semiconductor. First, if we assume charge transport is dominated by transitions between localized states above/below the valence/conduction band mobility edges, as in the case of hopping conduction, we can relate conductivity to the transition probability for hopping between sites. Based on the percolation theory model, which states that conduction is dominated not by the average distance between sites, but by a critical distance at which hopping rates are at their lowest while still allowing for a continuous transport path through the solid, conductivity (specifically, mobility) can be defined as proportional to $\exp(-\gamma/\alpha N^{1/3})$, where γ is a factor and N is the concentration of sites, and is expected to

increase with increasing N .^{136,137} Therefore, assuming a correlation between concentration of sites and concentration of atoms in the solid (i.e., density), we might expect that decreasing density would lead to decreasing conductivity (i.e., higher resistivity), as is indeed observed in a-B_xC:H_y at H concentrations <35%. Another way to look at the problem might be to consider a multiple trapping and release mechanism, where conduction occurs via extended band states, but conductivity (specifically, mobility) is reduced through trapping by localized states. In this scenario, we can assume that resistivity would be related to disorder, represented by the Urbach energy and Tauc slope parameter. A higher Urbach energy implies a wider Urbach tail, and consequently increased trapping by localized states and lower conductivity (higher resistivity). This reasoning is typically applied to amorphous silicon in relating narrower band tails to higher mobilities and thus better device quality.^{60,138,139} Because this relationship between Urbach energy and resistivity is not observed in the regime of 10%–35% at. % H, this suggests that a hopping/percolation model better describes the data at low hydrogen concentrations in a-B_xC:H_y. This is reasonable considering the fact that at low H concentrations, the band gap is at its lowest (~2 eV), but the Urbach energy is at its highest (~700 meV), implying that localized tail states fill the majority of the gap. The reversal in trend between resistivity and at. % H observed at ~35% H may suggest a transition from a hopping to a multiple trapping mechanism. In this stoichiometric regime, the Urbach energy is much lower, and therefore the band tails much narrower. A similar transition in transport mechanisms is proposed for a-SiC:H as a function of C fraction, although not necessarily for identical reasons.¹⁴⁰

V. CONCLUSIONS

We have investigated the relationship between chemical, physical/mechanical, optical/electronic, and electrical transport properties in amorphous hydrogenated boron carbide, and have shown that hydrogenation has a clear and powerful effect on material properties important for technological applications. Through varying growth temperature and power, we have demonstrated that a wide range of properties can be obtained in PECVD *ortho*-carborane-based a-B_xC:H_y films, including atomic concentration hydrogen from 10% to 45%, density from 0.9 to 2.3 g/cm³, hardness from 1 to 25 GPa, Young's modulus from 10 to 340 GPa, dielectric constant (κ) from 3.1 to 7.6, Tauc band gap (E_{Tauc} , $n=2$) from 1.7 to 3.8 eV, Tauc slope parameter ($B^{1/2}$) from ~200 to 1600 cm^{-1/2} eV^{-1/2}, Urbach energy (E_U) from 0.1 to 0.7 eV, and electrical resistivity from 10¹⁰ to 10¹⁵ Ω cm. The low dielectric constant, excellent mechanical strength, low pore interconnectivity, and high resistivity/low leakage current in these films are promising toward their use in insulating low- κ dielectric applications. Further, the sensitive tunability of their optical, electronic, and electrical transport properties suggests avenues for optimization toward other specialized electronic applications such as neutron detection.

We have identified two extremes of material composition within the growth regime studied: at low growth temperature and power, a hydrogen-rich, low-density film is formed, and at high growth temperature and power, a hydrogen-deficient, high-density film is formed. Hydrogen and density demonstrate a very clear inverse linear correlation with each other, and map many of the other material properties. Lower density films exhibit low hardness and Young's modulus, high band gap, low E_U /high $B^{1/2}$ (i.e., low disorder), low dielectric constant, and high electrical resistivity, while the opposite is true for the higher density films. We have analyzed the trends in the context of classic amorphous systems including a-Si:H, a-C:H, and a-SiC:H, and have found that, despite its very different atomic structure (i.e., six-fold icosahedral coordinate vs four-fold tetrahedral coordinate), a-B_xC:H_y exhibits many similarities to these systems, especially a-Si:H. We propose that hydrogenation of the a-B_xC:H_y network has several key effects: (1) it decreases network connectivity and average coordination number, which affects E , H , E_g , ϵ_1/κ , and ρ ; (2) it decreases mass/electron density, which is also directly related to ϵ_1/κ ; and finally, (3) it relieves strain in the network, which results in a decrease in structural disorder as measured by E_U and $B^{1/2}$. Regarding (1), the identification of a rigidity percolation threshold in a six-coordinate network is a novel finding that provides an interesting basis for future studies. Regarding (2), we note that in a-B_xC:H_y, E_U and E_g show an inverse correlation like in a-Si:H, which is opposite to the direct correlation between the two observed in a-C:H and a-SiC:H. Finally, we tentatively propose the possibility of a transition between hopping and multiple trapping transport mechanisms at a hydrogen concentration of ~35% based on the relationship between electrical resistivity and at. % H.

This study has provided a snapshot of process-parameter space for a-B_xC:H_y, and—within a fairly narrow process space—this material has already demonstrated significant tunability as well as very clear correlations between process, structure, and properties. Future work will investigate a wider range of process conditions, including variations in pressure and flow rate, as well as delve deeper into the analysis of atomic and electronic structure, and their relationship to mechanical, optical, and electrical properties. We anticipate that, as in the case of a-Si:H, rigorous efforts to understand and optimize this material will pay dividends towards its integration into viable commercial technologies.

ACKNOWLEDGMENTS

The authors gratefully acknowledge Intel Corporation (Contract No. 2012-IN-2313) and the Defense Threat Reduction Agency (Grant No. HDTRA1-10-1-0092) for financial support of this research.

¹D. Emin, *Phys. Today* **40**(1), 55 (1987).

²D. Emin, *J. Solid State Chem.* **179**, 2791 (2006).

³H. Werheit, *J. Phys.: Conf. Ser.* **176**, 012019 (2009).

⁴M. M. Balakrishnarajan, P. D. Pancharatna, and R. Hoffmann, *New J. Chem.* **31**, 473 (2007).

⁵V. Dornich, S. Reynaud, R. A. Haber, and M. Chhowalla, *J. Am. Ceram. Soc.* **94**, 3605 (2011).

- ⁶K. M. Reddy, P. Liu, A. Hirata, T. Fujita, and M. W. Chen, *Nat. Commun.* **4**, 2483 (2013).
- ⁷B. W. Robertson, S. Adenwalla, A. Harken, P. Welsch, J. I. Brand, P. A. Dowben, and J. P. Claassen, *Appl. Phys. Lett.* **80**, 3644 (2002).
- ⁸D. Emin and T. L. Aselage, *J. Appl. Phys.* **97**, 013529 (2005).
- ⁹A. N. Caruso, P. Dowben, S. Balkir, N. Schemm, K. Osberg, R. Fairchild, O. Flores, S. Balaz, A. Harken, and B. Robertson, *Mater. Sci. Eng., B* **135**, 129 (2006).
- ¹⁰N. Hong, J. Mullins, K. Foreman, and S. Adenwalla, *J. Phys. D: Appl. Phys.* **43**, 275101 (2010).
- ¹¹A. N. Caruso, *J. Phys.: Condens. Matter* **22**, 443201 (2010).
- ¹²L. M. Han, Y. Xu, J. Z. Xie, M. S. Zhou, and S. Chooi, "Use of boron carbide as an etch-stop and barrier layer for copper dual damascene metallization," U.S. patent 6,352,921 B1 (Mar. 5, 2002).
- ¹³S. W. King, *ECS J. Solid State Sci. Technol.* **4**, N3029 (2015).
- ¹⁴S. Vepřek, *Plasma Chem. Plasma Process.* **12**, 219 (1992).
- ¹⁵R. A. Keski-Kuha, G. M. Blumenstock, C. M. Fleetwood, and D.-R. Schmitt, *Appl. Opt.* **37**, 8038 (1998).
- ¹⁶Y. Chen, Y.-W. Chung, and S.-Y. Li, *Surf. Coat. Technol.* **200**, 4072 (2006).
- ¹⁷H. Hu and J. Kong, *J. Mater. Eng. Perform.* **23**, 651 (2014).
- ¹⁸F. Thévenot, *J. Eur. Ceram. Soc.* **6**, 205 (1990).
- ¹⁹A. K. Suri, C. Subramanian, J. K. Sonber, and T. S. R. C. Murthy, *Int. Mater. Rev.* **55**, 4 (2010).
- ²⁰M. Beauvy, *J. Less-Common Met.* **90**, 169 (1983).
- ²¹G. Fanchini, J. McCauley, and M. Chhowalla, *Phys. Rev. Lett.* **97**, 035502 (2006).
- ²²P. G. Debenedetti and F. H. Stillinger, *Nature* **410**, 259 (2001).
- ²³M. W. Chen, J. W. McCauley, J. C. LaSalvia, and K. J. Hemker, *J. Am. Ceram. Soc.* **88**, 1935 (2005).
- ²⁴J. E. Zorzi, C. A. Perottoni, and J. A. H. da Jornada, *Mater. Lett.* **59**, 2932 (2005).
- ²⁵S. Hayun, S. Kalabukhov, V. Ezersky, M. P. Dariel, and N. Frage, *Ceram. Int.* **36**, 451 (2010).
- ²⁶C. Wood and D. Emin, *Phys. Rev. B* **29**, 4582 (1984).
- ²⁷A. K. Bandyopadhyay, F. Beuneu, L. Zuppiroli, and M. Beauvy, *J. Phys. Chem. Solids* **45**, 207 (1984).
- ²⁸S. Lee, J. Mazurowski, G. Ramseyer, and P. A. Dowben, *J. Appl. Phys.* **72**, 4925 (1992).
- ²⁹G. M. Blumenstock and R. A. M. Keski-Kuha, *Appl. Opt.* **33**, 5962 (1994).
- ³⁰T. Hu, L. Steihl, W. Rafaniello, T. Fawcett, D. D. Hawn, J. G. Mashall, S. J. Rozeveld, C. L. Putzig, J. H. Blackson, W. Cermignani, and M. G. Robinson, *Thin Solid Films* **332**, 80 (1998).
- ³¹A. O. Sezer and J. I. Brand, *Mater. Sci. Eng., B* **79**, 191 (2001).
- ³²H. Suematsu, K. Kitajima, T. Suzuki, W. Jiang, K. Yatsui, K. Kurashima, and Y. Bando, *Appl. Phys. Lett.* **80**, 1153 (2002).
- ³³L. G. Jacobssohn, R. D. Averitt, C. J. Wetteland, R. K. Schulze, M. Nastasi, L. L. Daemen, Z. Jenei, and P. Asoka-Kumar, *Appl. Phys. Lett.* **84**, 4173 (2004).
- ³⁴S. Sasaki, M. Takeda, K. Yokoyama, T. Miura, T. Suzuki, H. Suematsu, W. Jiang, and K. Yatsui, *Sci. Technol. Adv. Mater.* **6**, 181 (2005).
- ³⁵V. K. Alimov, D. B. Bogomolov, M. N. Churaeva, A. E. Gorodetsky, S. L. Kanashenko, A. I. Kanaev, S. Y. Rybakov, V. M. Sharapov, A. P. Zakharov, R. K. Zalavutdinov, O. I. Buzhinsky, A. P. Chernobay, S. A. Grashin, S. V. Mirnov, V. I. Bregadze, and A. Y. Usyatinsky, *J. Nucl. Mater.* **196–198**, 670 (1992).
- ³⁶A. I. Kanaev, S. Y. Rybakov, and M. N. Churaeva, *Le J. Phys. IV* **3**, C3-183 (1993).
- ³⁷D. Byun, S.-D. Hwang, P. A. Dowben, F. K. Perkins, F. Filips, and N. J. Ianno, *Appl. Phys. Lett.* **64**, 1968 (1994).
- ³⁸V. M. Sharapov, S. V. Mirnov, S. A. Grashin, S. V. Lebedev, I. A. Kovan, A. V. Krasilnikov, V. A. Krupin, L. S. Levin, A. N. Romannikov, and A. P. Zakharov, *J. Nucl. Mater.* **220–222**, 730 (1995).
- ³⁹D. Zhang, D. N. McIlroy, W. L. O'Brien, and G. de Stasio, *J. Mater. Sci.* **33**, 4911 (1998).
- ⁴⁰D. N. McIlroy, S.-D. Hwang, K. Yang, N. Remmes, P. A. Dowben, A. A. Ahmad, N. J. Ianno, J. Z. Li, J. Y. Lin, and H. X. Jiang, *Appl. Phys. A: Mater. Sci. Process.* **67**, 335 (1998).
- ⁴¹S. Adenwalla, P. Welsch, A. Harken, J. I. Brand, A. Sezer, and B. W. Robertson, *Appl. Phys. Lett.* **79**, 4357 (2001).
- ⁴²A. N. Caruso, R. B. Billa, S. Balaz, J. I. Brand, and P. A. Dowben, *J. Phys.: Condens. Matter* **16**, L139 (2004).
- ⁴³D. L. Schulz, A. Lutfurakhmanov, B. Mayo, J. Sandstrom, D. Bunzow, S. B. Qadri, R. Bao, D. B. Chrisey, and A. N. Caruso, *J. Non-Cryst. Solids* **354**, 2369 (2008).
- ⁴⁴R. B. Billa, T. Hofmann, M. Schubert, and B. W. Robertson, *J. Appl. Phys.* **106**, 033515 (2009).
- ⁴⁵R. A. Street, *Hydrogenated Amorphous Silicon* (Cambridge University Press, New York, 1991).
- ⁴⁶*Technology and Applications of Amorphous Silicon*, edited by R. A. Street (Springer, New York, 2000).
- ⁴⁷P. Roca i Cabarrocas, *Curr. Opin. Solid State Mater. Sci.* **6**, 439 (2002).
- ⁴⁸A. F. M. Leenaars, J. A. M. Huethorst, and J. J. van Oekel, *Langmuir* **6**, 1701 (1990).
- ⁴⁹A. A. Ahmad, N. J. Ianno, P. G. Snyder, D. Welipitiya, D. Byun, and P. A. Dowben, *J. Appl. Phys.* **79**, 8643 (1996).
- ⁵⁰F. Wooten, *Optical Properties of Solids* (Academic Press, New York, 1972).
- ⁵¹W. A. Lanford, H. P. Trautvetter, J. F. Ziegler, and J. Keller, *Appl. Phys. Lett.* **28**, 566 (1976).
- ⁵²S. W. King, L. Ross, H. Li, G. Xu, J. Bielefeld, R. E. Atkins, P. D. Henneghan, K. Davis, D. C. Johnson, and W. A. Lanford, *J. Non-Cryst. Solids* **389**, 78 (2014).
- ⁵³D. Koh, J.-H. Yum, S. K. Banerjee, T. W. Hudnall, C. Bielawski, W. A. Lanford, B. L. French, M. French, P. Henry, H. Li, M. Kuhn, and S. W. King, *J. Vac. Sci. Technol., B* **32**, 03D117 (2014).
- ⁵⁴Y. Lin, Y. Xiang, T. Y. Tsui, and J. J. Vlassak, *Acta Mater.* **56**, 4932 (2008).
- ⁵⁵ISO 14577-4, *Metallic Materials—Instrumented Indentation Tests for Hardness and Materials Parameters, Part 4: Test Methods for Metallic and Non-Metallic Coatings* (ISO, Geneva, Switzerland, 2007).
- ⁵⁶D. W. Gidley, H.-G. Peng, and R. S. Vallery, *Annu. Rev. Mater. Res.* **36**, 49 (2006).
- ⁵⁷G. Hodes, *Chemical Solution Deposition of Semiconductor Films* (Marcel Dekker, Inc., 2003).
- ⁵⁸D. L. Wood and J. Tauc, *Phys. Rev. B* **5**, 3144 (1972).
- ⁵⁹D. E. Sweenor, S. K. O'Leary, and B. E. Foutz, *Solid State Commun.* **110**, 281 (1999).
- ⁶⁰G. D. Cody, T. Tiedje, B. Abeles, B. Brooks, and Y. Goldstein, *Phys. Rev. Lett.* **47**, 1480 (1981).
- ⁶¹G. D. Cody, *J. Non-Cryst. Solids* **141**, 3 (1992).
- ⁶²G. F. Silva, F. L. Camargo, and A. L. O. Ferreira, *Fuel Process. Technol.* **92**, 407 (2011).
- ⁶³S. Ghosh, P. K. Dutta, and D. N. Bose, *Mater. Sci. Semicond. Process.* **2**, 1 (1999).
- ⁶⁴M. Li, G. Li, and S. Azarm, *J. Mech. Des.* **130**, 031401 (2008).
- ⁶⁵J. P. C. Kleijnen, *Eur. J. Oper. Res.* **192**, 707 (2009).
- ⁶⁶See supplementary material at <http://dx.doi.org/10.1063/1.4927037> for IV vs density data.
- ⁶⁷J. I. Onate, A. Garcia, V. Bellido, and J. L. Viviente, *Surf. Coat. Technol.* **49**, 548 (1991).
- ⁶⁸A. Annen, *Thin Solid Films* **312**, 147 (1998).
- ⁶⁹P. Chaudhari, N. Meshram, A. Singh, A. Topkar, and R. Dusane, *Thin Solid Films* **519**, 4561 (2011).
- ⁷⁰M. Saß, A. Annen, and W. Jacob, *J. Appl. Phys.* **82**, 1905 (1997).
- ⁷¹R. Paroli, N. Kawai, and G. Lord, *Inorg. Chem.* **28**, 1819 (1989).
- ⁷²M. Weiler, S. Sattel, T. Giessen, and K. Jung, *Phys. Rev. B* **53**, 1594 (1996).
- ⁷³J. Robertson, *Mater. Sci. Eng., R* **37**, 129 (2002).
- ⁷⁴M. M. Paquette, W. Li, M. Sky Driver, S. Karki, A. N. Caruso, and N. A. Oyler, *J. Phys.: Condens. Matter* **23**, 435002 (2011).
- ⁷⁵H. Werheit, U. Kuhlmann, H. W. Rotter, and S. O. Shalamberidze, *J. Phys.: Condens. Matter* **22**, 395401 (2010).
- ⁷⁶D. Peak, G. W. Luther III, and D. L. Sparks, *Geochim. Cosmochim. Acta* **67**, 2551 (2003).
- ⁷⁷O. Moon, B. Kang, S. Lee, and J. Boo, *Thin Solid Films* **464–465**, 164 (2004).
- ⁷⁸K. Shirai, S. Emura, S. Gonda, and Y. Kumashiro, *J. Appl. Phys.* **78**, 3392 (1995).
- ⁷⁹S.-H. Lin and B. J. Feldman, in *Symposium F - Wide Bandgap Semiconductors for High Power, High Frequency*, edited by J. A. Bain, D. Bogy, M. Levy, J. P. Lorenzo, M. Mansuripur, T. Nolan, Y. Ok, K. Rubin, and B. J. H. Stadler (Mater. Res. Soc. Symp. Proc., 1998), Vol. 517, p. 433.
- ⁸⁰A. Grill and D. A. Neumayer, *J. Appl. Phys.* **94**, 6697 (2003).

- ⁸¹B. H. Stuart, *Infrared Spectroscopy: Fundamentals and Applications* (John Wiley & Sons, Ltd., Chichester, UK, 2004).
- ⁸²S. W. King, M. French, J. Bielefeld, and W. A. Lanford, *J. Non-Cryst. Solids* **357**, 2970 (2011).
- ⁸³D. K. Basa, *Thin Solid Films* **406**, 75 (2002).
- ⁸⁴A. Hori, M. Takeda, H. Yamashita, and K. Kimura, *J. Phys. Soc. Jpn.* **64**, 3496 (1995).
- ⁸⁵A. R. Forouhi and I. Bloomer, *Phys. Rev. B* **34**, 7018 (1986).
- ⁸⁶A. Zanatta and I. Chambouleyron, *Phys. Rev. B: Condens. Matter* **53**, 3833 (1996).
- ⁸⁷P. Lunca-Popa, J. I. Brand, S. Balaz, L. G. Rosa, N. M. Boag, M. Bai, B. W. Robertson, and P. A. Dowben, *J. Phys. D: Appl. Phys.* **38**, 1248 (2005).
- ⁸⁸A. S. Anan'ev, O. I. Kon'kov, V. M. Lebedev, A. N. Novokhatski, E. I. Terukov, and I. N. Trapeznikova, *Semiconductors* **36**, 941 (2002).
- ⁸⁹J. Müllerová, L. Průšáková, M. Netrvalová, V. Vavrušková, and P. Šutta, *Appl. Surf. Sci.* **256**, 5667 (2010).
- ⁹⁰G. B. Tong, Z. Aspanut, M. R. Muhamad, and S. Abdul Rahman, *Vacuum* **86**, 1195 (2012).
- ⁹¹A. Arrais, P. Benzi, E. Bottizzo, and C. Demaria, *J. Phys. D: Appl. Phys.* **42**, 105406 (2009).
- ⁹²G. Ambrosone, D. K. Basa, U. Coscia, and P. Rava, *Thin Solid Films* **518**, 5871 (2010).
- ⁹³B. P. Swain, S. B. Patil, A. Kumbhar, and R. O. Dusane, *Thin Solid Films* **430**, 186 (2003).
- ⁹⁴K. Tanaka, *J. Non-Cryst. Solids* **389**, 35 (2014).
- ⁹⁵G. Fanchini and A. Tagliaferro, *Appl. Phys. Lett.* **85**, 730 (2004).
- ⁹⁶P. A. Kohl, *Annu. Rev. Chem. Biomol. Eng.* **2**, 379 (2011).
- ⁹⁷G. Samara, H. Tardy, E. Venturini, T. Aselage, and D. Emin, *Phys. Rev. B: Condens. Matter* **48**, 1468 (1993).
- ⁹⁸F. Volpi, M. Braccini, A. Devos, G. Raymond, A. Pasturel, and P. Morin, *J. Appl. Phys.* **116**, 043506 (2014).
- ⁹⁹C. Manfredotti, F. Fizzotti, M. Boero, P. Pastorino, P. Polesello, and E. Vittone, *Phys. Rev. B* **50**, 18046 (1994).
- ¹⁰⁰A. H. M. Smets, W. M. M. Kessels, and M. C. M. Van de Sanden, *Appl. Phys. Lett.* **82**, 1547 (2003).
- ¹⁰¹C. Casiraghi, A. Ferrari, and J. Robertson, *Phys. Rev. B* **72**, 1 (2005).
- ¹⁰²D. K. Basa, G. Abbate, G. Ambrosone, U. Coscia, and A. Marino, *J. Appl. Phys.* **107**, 023502 (2010).
- ¹⁰³A. M. Wrobel, A. Walkiewicz-Pietrzykowska, P. Uznanski, and B. Glebocki, *Thin Solid Films* **520**, 7100 (2012).
- ¹⁰⁴S. W. King, J. Bielefeld, G. Xu, W. A. Lanford, Y. Matsuda, R. H. Dauskardt, N. Kim, D. Hondongwa, L. Olasov, B. Daly, G. Stan, M. Liu, D. Dutta, and D. Gidley, *J. Non-Cryst. Solids* **379**, 67 (2013).
- ¹⁰⁵S. Kageyama, N. Matsuki, and H. Fujiwara, *J. Appl. Phys.* **114**, 233513 (2013).
- ¹⁰⁶H. Fan, C. Hartshorn, T. Buchheit, D. Tallant, R. Assink, R. Simpson, D. J. Kissel, D. J. Lacks, S. Torquato, and C. J. Brinker, *Nat. Mater.* **6**, 418 (2007).
- ¹⁰⁷H.-S. Ma, A. P. Roberts, J.-H. Prévost, R. Jullien, and G. W. Scherer, *J. Non-Cryst. Solids* **277**, 127 (2000).
- ¹⁰⁸H. He and M. Thorpe, *Phys. Rev. Lett.* **54**, 2107 (1985).
- ¹⁰⁹M. F. Thorpe, D. J. Jacobs, N. V. Chubynsky, and A. J. Rader, "Generic rigidity of network glasses," in *Rigidity Theory and Applications* (Springer, New York, 2002), pp. 239–277.
- ¹¹⁰J. C. Mauro, *Am. Ceram. Soc. Bull.* **90**, 31 (2011).
- ¹¹¹R. Zallen, *The Physics of Amorphous Solids* (John Wiley & Sons, Inc., New York, 1998).
- ¹¹²P. Boolchand and M. F. Thorpe, *Phys. Rev. B* **50**, 10366 (1994).
- ¹¹³P. Boolchand, M. Zhang, and B. Goodman, *Phys. Rev. B* **53**, 11488 (1996).
- ¹¹⁴H. M. Pastawski, L. S. De Bernardez, and J. F. Weisz, *Phys. Rev. B* **32**, 5468 (1985).
- ¹¹⁵D. A. Papaconstantopoulos and E. N. Economou, *Phys. Rev. B* **24**, 7233 (1981).
- ¹¹⁶A. H. Mahan, R. Biswas, L. M. Gedvilas, D. L. Williamson, and B. C. Pan, *J. Appl. Phys.* **96**, 3818 (2004).
- ¹¹⁷M. Legesse, M. Nolan, and G. Fagas, *J. Phys. Chem. C* **117**, 23956 (2013).
- ¹¹⁸I. Solomon, *Appl. Surf. Sci.* **184**, 3 (2001).
- ¹¹⁹J. Robertson, *Philos. Mag. B* **66**, 615 (1992).
- ¹²⁰B. Akaoglu, K. Sel, I. Atilgan, and B. Katircioglu, *Opt. Mater.* **30**, 1257 (2008).
- ¹²¹G. Ambrosone, D. K. Basa, U. Coscia, and M. Fathallah, *J. Appl. Phys.* **104**, 123520 (2008).
- ¹²²P. D. Persans, A. F. Ruppert, S. S. Chan, and G. D. Cody, *Solid State Commun.* **51**, 203 (1984).
- ¹²³C. Mathioudakis, G. Kopidakis, P. Patsalas, and P. C. Kelires, *Diamond Relat. Mater.* **16**, 1788 (2007).
- ¹²⁴A. H. Mahan, P. Menna, and R. Tsu, *Appl. Phys. Lett.* **51**, 1167 (1987).
- ¹²⁵F. Finocchi and G. Galli, *Phys. Rev. B* **50**, 7393 (1994).
- ¹²⁶C. R. S. da Silva, J. F. Justo, and A. Fazzio, *Phys. Rev. B* **65**, 1 (2002).
- ¹²⁷C. R. S. da Silva, J. F. Justo, and A. Fazzio, *J. Non-Cryst. Solids* **338–340**, 299 (2004).
- ¹²⁸A. R. Zanatta, M. Mulato, and I. Chambouleyron, *J. Appl. Phys.* **84**, 5184 (1998).
- ¹²⁹Y. Pan, F. Inam, M. Zhang, and D. Drabold, *Phys. Rev. Lett.* **100**, 206403 (2008).
- ¹³⁰R. Tsu, P. Menna, and A. H. Mahan, *Sol. Cells* **21**, 189 (1987).
- ¹³¹M. H. Brodsky and P. J. Stiles, *Phys. Rev. Lett.* **25**, 798 (1970).
- ¹³²K. Maex, M. R. Baklanov, D. Shamiryan, F. Lacopi, S. H. Brongersma, and Z. S. Yanovitskaya, *J. Appl. Phys.* **93**, 8793 (2003).
- ¹³³R. R. Reddy, K. R. Gopal, K. Narasimhulu, L. S. S. Reddy, K. R. Kumar, G. Balakrishnaiah, and M. R. Kumar, *J. Alloys Compd.* **473**, 28 (2009).
- ¹³⁴N. Maley, *Phys. Rev. B* **46**, 2078 (1992).
- ¹³⁵S. Kageyama, M. Akagawa, and H. Fujiwara, *Phys. Rev. B* **83**, 195205 (2011).
- ¹³⁶S. Baranovski, *Charge Transport in Disordered Solids with Applications in Electronics* (Wiley, Hoboken, NJ, 2006).
- ¹³⁷S. D. Baranovskii, *Phys. Status Solidi B* **251**, 487 (2014).
- ¹³⁸D. S. Shen and S. Wagner, *J. Appl. Phys.* **79**, 794 (1996).
- ¹³⁹E. A. Schiff, *Sol. Energy Mater. Sol. Cells* **78**, 567 (2003).
- ¹⁴⁰V. Chu, J. P. Conde, J. Jarego, P. Brogueira, J. Rodriguez, N. Barradas, and J. C. Soares, *J. Appl. Phys.* **78**, 3164 (1995).